Endbericht

Engineering Marangoni Flows (EMA)

Project Nummer 819714, ASAP6

Berichtszeitraum:

01.07.2009 – 31.12.2010

Hendrik Kuhlmann, Michael Lukasser und Frank Muldoon
Institut für Strömungsmechanik und Wärmeübertragung
Technische Universität Wien

19 Juli 2011

Zusammenfassung

Dieser Abschlussbericht dokumentiert die Arbeiten, die innerhalb des Projekts *Engineering Marangoni Flows* im Zeitraum vom 1. Juli 2009 bis zum 31. Dezember 2010 durchgeführt wurden. Das Projekt befasst sich mit der Entwicklung numerischer Methoden und der Berechnung von Daten zur Strömung in einer nichtisothermen Flüssigkeitsbrücke. Hierzu wird die Reynoldszahl für den Einsatzpunkt (kritischer Punkt) von dreidimensionalen Hydrothermalwellen berechnet, superkritische Simulationen durchgeführt und die Dynamik suspendierter Partikel untersucht. Insbesondere wird der Einfluss einer koaxialen Gasströmung auf den kritischen Punkt berechnet. Die Arbeiten dienen dem JEREMI-Experiment, welches ab 2015 auf der Internationalen Raumstation durchgeführt werden soll.

Um die verschiedenen Einflussfaktoren auf die Stabilität der Grundsrömung zu bestimmen, wurden umfangreiche Stabilitätsgrenzen berechnet. Es zeigt sich, dass die kritischen Reynoldszahlen sehr stark von den Material- und Geometrieparametern abhängen. Insbesondere wird eine Restabilisierung gefunden. Damit ist es im Prinzip möglich, dass die Hydrothermalwellen bei hoher Reynoldszahl wieder zugunsten einer axisymmetrischen Grundströmung unterdrückt werden. Auch kann eine komplexe nichtlineare Dynamik die Folge sein.

Die Strömung in Flüssigkeitsbrücken wurden mit drei verschiedene Softwarepaketen erfolgreich simuliert. Dazu wurden Fluent©, OpenFOAM© and Nek5000 verwendet. Simulationen mit deformierter freier Oberfläche wurden mit dem Softwarepaket OpenFOAM© durchgeführt, welches die freie Oberfläche sharf abbildet (*sharp-interface method*).

Darüber hinaus wurde ein Code zur Berechnung der Trajektorien von kleinen Partikeln geschrieben, die sich in der thermokapillaren Strömung bewegen. Zweckmäßigerweise geschieht dies in einem rotierenden Koordinatenssytem, welches sich mit der Hydrothermalwelle mitbewegt. Es konnte gezeigt werden, dass die Wechselwirkung zwischen einzelnen bewegten Teilchen und der freien Grenzfläche ein sehr effizienter Mechanismus ist, der zu einer Entmischung und zu Partikelakkumulationsstrukturen führen kann. Die gefundenen Muster sind in qualitativer Übereinstimmung mit entsprechenden experimenten Befunden. Von besonderer Bedeutung für das JEREMI-Projekt ist die korrekte Abbildung der Zeitskalen (wie im Experiment unter 1g), die für die Entmischung der Partikel erforderlich ist.

Abstract

This final report covers the work which has been carried out within the project *Engineering Marangoni Flows* in the period from July 1, 2009 to December 31, 2010. The project is concerned with the development of numerical methods for and the computation of flows in a non-isothermal liquid bridge. To that end the Reynolds number for the onset (critical point) of three-dimensional hydrothermal waves is computed, three-dimensional numerical simulations carried out, and the dynamics of liquid-suspended particles are studied. In particular, the influence of a coaxial gas flow on the critical point is investigated. These investigations are in support of the JEREMI experiment which is planned to be carried out onboard the International Space Station beginning in 2015.

In order to investigate the various factors influencing the stability of the basic flow, comprehensive stability boundaries have been calculated. The critical Reynolds numbers were found to strongly depend on the material and geometry parameters. In particular, a re-stabilization of the basic flow has been discovered. Therefore, it is possible that hydrothermal waves are suppressed in favor of the steady axisymmetric state even if the Reynolds number is increased. Moreover, a complex nonlinear dynamics may result.

Simulations of the flow and heat transfer in the liquid bridge have been successfully carried out using three independent software packages; Fluent©, OpenFOAM© and Nek5000. These simulations have included modeling of the deformation of the free surface with the software package OpenFOAM© using a sharp interface method.

A numerical code was developed which calculates the trajectories of particles moving in the thermocapillary flow. It is of advantage to do this in the rotating frame of reference that moves with the hydrothermal wave. It was shown that the interaction between individual moving particles and the liquid–gas interface represents a very efficient mechanism to de-mix and form particle accumulation structures. The patterns found numerically are in qualitative agreement with corresponding experimental results and more importantly for the experiments supported by this work, the particle model is able to reproduce particle accumulation structures on the time scale found in other (ground based) experiments.

Contents

1 Preface

The report is structured according to the work packages which have been defined in the original proposal. In order to indicate the perspective of the project in case of a successor project some work packages have been described which should not, or only partially, be covered during the 18 month period of the project duration. For these reasons work packages A3.1–A4.3, B4.3–B4.4, and C4.3 are not a subject of this report. Since the successor project (EMA2) was rejected, it did not make sense to begin these work packages.

In the course of the negotiation for the contract the budget has been reduced significantly. As a result, only two scientists, instead of the three which were originally foreseen and which were required for the project, were funded. This shortfall has been moderated by additional resources of TUWien and by a mutual agreement concerning the cancelation of work packages C2.1 and C2.2 which, likewise are not reported here.

The remaining work packages scheduled for the period of 18 months are nearly fully completed. In the following the individual work packages are addressed describing their status, results of the work done and changes, if applicable.

1.1 Resource shifting: WP A

Since the work packages A4.1–A.4.3 and C4.3 were planned to be treated only after this project they are not subject of this report. Two months of work have been foreseen for the work package A3.1. As it this work package could not have been finished within the period of this project and because it has been found that this line of work represented a less efficient and accurate means of determining the stability boundaries as compared to that offered by the development of `MaranStable` in WP B1.1–B2.3 the remaining time (2 months) has been used in WP C3.1–C4.4.

1.2 Resource shifting: WP B

In the course of WP B1.1–B2.3, it was discovered that a re-stabilization of the basic flow occurs. This unexpected result has never been reported in the literature on liquid bridges. Such a re-stabilization can have a profound impact on the experimental realization and is particularly important for the space experiment. Therefore, more time was required to develop the tool `MaranStable` and to fully capture the re-stabilization zones which turned out to be quite convoluted. The

required time was taken from WP B3.1–B4.2 as well as from the fraction of B4.3 which falls into this project period.

2 A: Simulation

WP A1.1: Literature review for 3D unsteady simulations

A large number of papers and books have been read.

WP A1.2: Setting up hardware

An eight-core workstation has been setup for model development. A 32-core cluster with 96 GB of memory has been installed for the production runs of the simulation tools.

WP A1.3: Introduction of OpenFOAM©

OpenFOAM© has been installed and been tested using elementary model problems. This has included running simulations on parallel machines.

Changes

Owing to the specific experience of Dr. Muldoon the software Fluent© was used for the first simulations. The software Nek5000 was also used, but was abandoned due to its unsuitability for such problems. OpenFOAM© is now being employed exclusively for realizing the 3D unsteady model of the flow. An important advantage to OpenFOAM© is the open access nature of the software, which eliminates any licensing and hence financial concerns, which are particularly important when doing parallel computing. A particular modeling advantage is the ability of the `SharpInterTrack` solver within OpenFOAM© to address moving interface problems using a sharp interface method. This approach is currently being used to model the combined gas–liquid problem with dynamic surface deformation. Due to the working assumption of our group that a key element of PAS formation is the result of collisions of the particles with the gas–liquid interface, the ability to accurately model the flow close to the interface is crucial. An alternative to a sharp interface method is a *single-fluid* method, such as Volume Of Fluid (VOF), where the interface is defined by a scalar function which has one value in the gas phase and a different value in the liquid phase. The interface is then defined by the region of the fluid where the value of the scalar function changes from the value of the gas

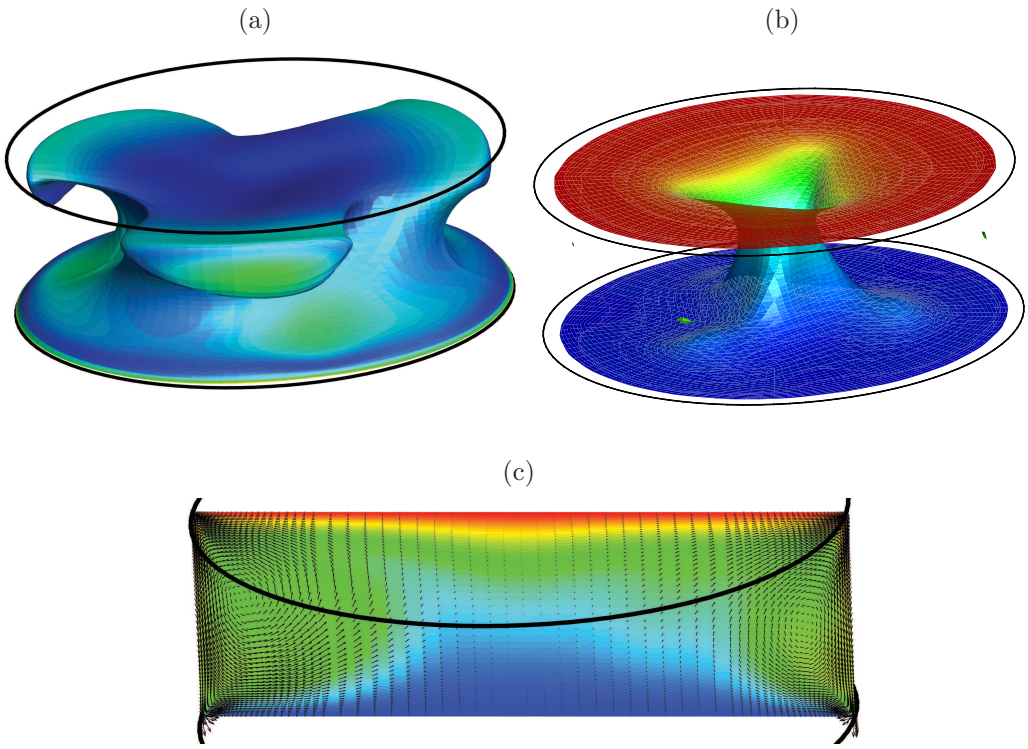

Figure 2.1: (a) Isosurface of the temperature field colored by velocity magnitude for the C-model at one instance in time. (b) Isosurface of the velocity field colored by temperature. (c) Instantaneous velocity and temperature field in a vertical cross section. The fields are shown for aspect ratio $\Gamma = 0.66$, $\mathrm{Re} = 1800$, $\mathrm{Pr} = 4$ and zero gravity. Results are from Fluent.

to the liquid value. A problem with this approach is that the scalar function does not have the correct discontinuous behavior at the interface, but is instead typically smeared over a distance equal to that of a few computational cells near the interface. Within the context of the JEREMI project, other groups have used the VOF approach for modeling the liquid bridge, but have had bad experiences, primarily relating to the excessive computational time required to accurately capture the interface, which requires an extremely fine mesh.

WP A2.1: Simulation of C-model

The C-Model is the three-dimensional temporally varying numerical representation of the governing equations for the liquid bridge without gas flow. The simulation has been carried out using Fluent, NEK5000 and OpenFOAM©. The results have been validated against results from the code Poseidon, written by Leypoldt *et al.* (2000). Validation of results from OpenFOAM© is in progress. It is worth noting that the OpenFOAM© solver used here is not `SharpInterTrack`, but is instead based on a

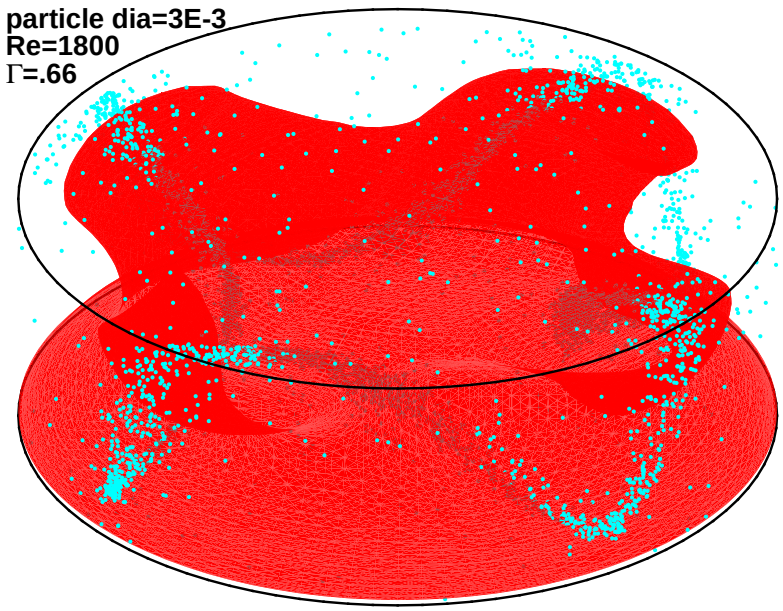

Figure 2.2: PAS using OpenFOAM©. The red iso-surface represents the mean temperature of the heaters, i.e. $T = (T_{\text{hot}} + T_{\text{cold}})/2$. The other parameters are $\Gamma = 0.66$, $\text{Re} = 1800$, $\text{Pr} = 4$ and zero gravity.

solver using a fixed grid, i.e., one that does not model surface deformations. Two views of a snapshot in time of a liquid bridge simulation are presented in fig. 2.1.

The three pronged traveling (rotating) wave can be clearly seen. The grid used was a fully hexahedral one with anisotropic grid clustering near the free surface to resolve the velocity gradients caused by the Marangoni stress. The simulation used a third order spatially and second order temporally accurate scheme. The coupled pressure-velocity solver of Fluent was used. The work in this work package has been extended by the need for highly resolved (and therefore computationally intensive) simulations to test a theory of PAS formation (see WP C4.2). These simulations are currently underway.

Work has also been done including modeling particle transport (i.e., PAS) using OpenFOAM©. This work is important as the code Poseidon is restricted to cylindrical geometries (i.e., the C-model). As the JEREMI experiment will be somewhat different as free-surface deformations will exist (and all terrestial experiments will have surface deformation due to gravity), the ability to model PAS in different geometries is very important. Figure 2.2 shows results of PAS from OpenFOAM©.

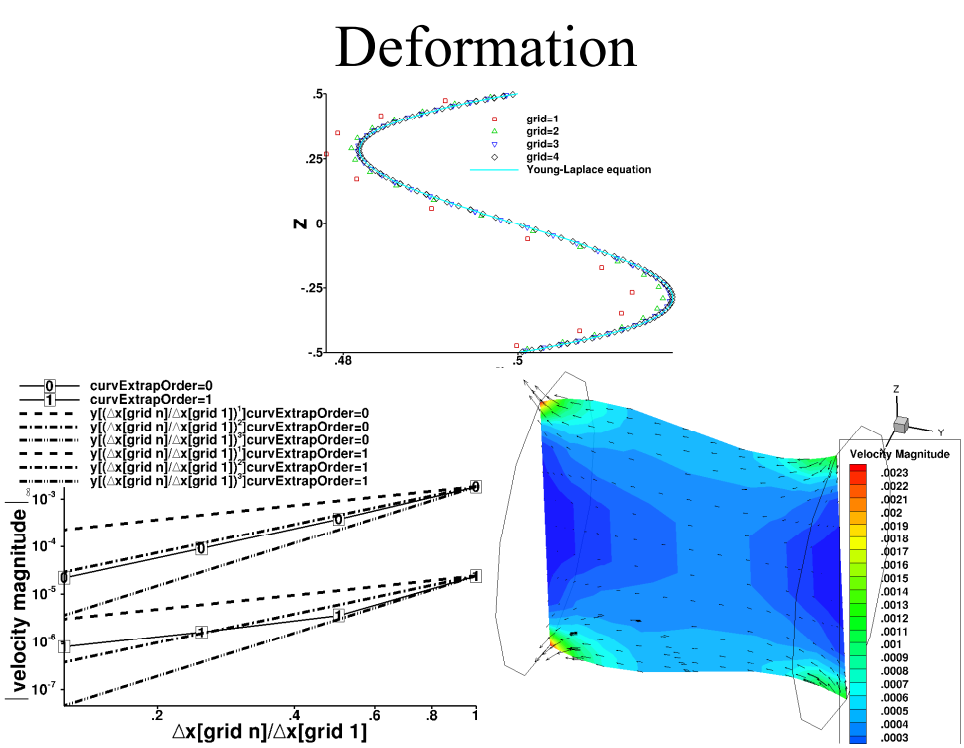

Figure 2.3: Addressing the issue of parasitic flow. Results obtained by using OpenFOAM© and `SharpInterTrack`.

WP A2.2: Simulation of CG-model

Changes

This model has been combined with the SG-model of WP A2.4, since the solver used (`SharpInterTrack`) has the ability to model dynamic deformation of the interface.

WP A2.3: Simulation of S-model

Deformation of the liquid bridge due to the influence of gravity has been done using the sharp interface solver `SharpInterTrack` of Dr. Tukovic from University of Zagreb. A particular issue with modeling flows with surface tension is that of *parasitic flows* which arise due to an imbalance between volume forces in the fluid and the surface force due to surface tension. This is a well known issue, and is particularly severe in VOF models. Such parasitic flows were also found using `SharpInterTrack` at the location where the interface contacted the walls. As the solver was primarily used for modeling freely rising bubbles which did not contact

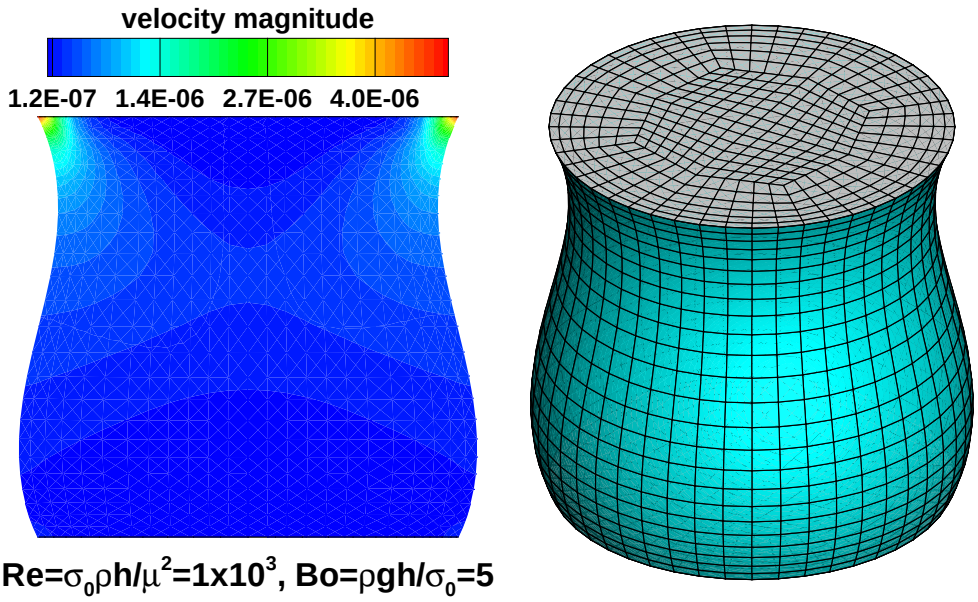

Figure 2.4: Deformation under the influence of gravity. Results obtained by using OpenFOAM© and `SharpInterTrack`.

walls, successfully addressing this problem required some changes to the solver, which was carried by Dr. Tukovic in close collaboration with our group. The result of this work, which was focused on a more accurate representation of the curvature at the wall, was the ability to reduce the parasitic flows to a very small level, the magnitude of which decreases with greater than second order accuracy as the grid is refined. This last feature is of prime importance, as it means that the parasitic flows can be reduced to any desired level by refining the grid. Figure 2.3 contains results from `SharpInterTrack` showing excellent agreement between it and the solution of the Young-Laplace equation. Figure 2.3 shows deformation under the influence of gravity using `SharpInterTrack`.

Current work is focused on addressing issues involved with applying the Marangoni stress within the `SharpInterTrack`.

WP A2.4: Simulation of SG-model

A grid has been built, using Gambit, which includes the gas and the liquid. This grid is of very high quality, being constructed entirely of hexahedral elements and including anisotropic grid refinement at the gas-liquid interface. Work is under way using `SharpInterTrack`. An issue currently holding up progress is that the application of the Marangoni force causes it to be very difficult to satisfy conservation of mass when using `SharpInterTrack`. When this issue is resolved, the result will be a solver capable of accurately modeling time-dependent deformation of the free

surface, which represents a much more accurate model of the liquid bridge than initially envisioned in the proposed work.

Changes

Approximately 25% of the time allotted to this WP has been shifted to WP A2.3 to address some issues with the dynamically deforming mesh method of `SharpInterTrack`.

WP A4.4: Dissemination of results

Results regarding the use of `SharpInterTrack` in liquid bridges including the surrounding gas phase were presented at the JEREMI and the spring meeting on March 7th in Brussels, see the section on presentations on page 43.

3 B: Stability

WP B1.1: Literature review for 3D stability

A large number of papers and books have been read to provide a theoretical background on flow stability and on numerical methods.

WP B1.2: Handling of the 3D stability code

Test calculations have been conducted with the steady 2D solver for the backward-facing-step problem. The aim was to become familiar with MATLAB, the structure of the code, the discretization and with the solution of steady 2D flow problems.

The work in this package is finished. The required knowledge for the next package has been acquired.

Changes

Due to the unforeseen change of the personnel (postdoc) the expertise of Dr. Schoisswohl who has written a dedicated 3D stability code for cylindrical geometries is no longer available. Therefore, we decided to modify another existing linear stability code. This code has been developed by Daniel Lanzerstorfer, another member of the group. The code is written in MATLAB instead of C. It is originally designed for structured Cartesian meshes and has been fully validated. The advantage of the new code is the employment of fast modern solution techniques for large linear system and large eigenvalue problems. MATLAB also has implemented a large number of built-in tools (solvers) which can be applied for the three-dimensional stability analysis.

WP B2.1: Program development for 3D stability and the CG-model

The above MATLAB code has been adapted to the cylindrical geometry. The calculation of the 2D basic state including the flow in the gas phase has been implemented.

In a first step isothermal steady 2D axisymmetric single-phase flow has been considered. To that end the steady 2D code for the backward-facing-step problem

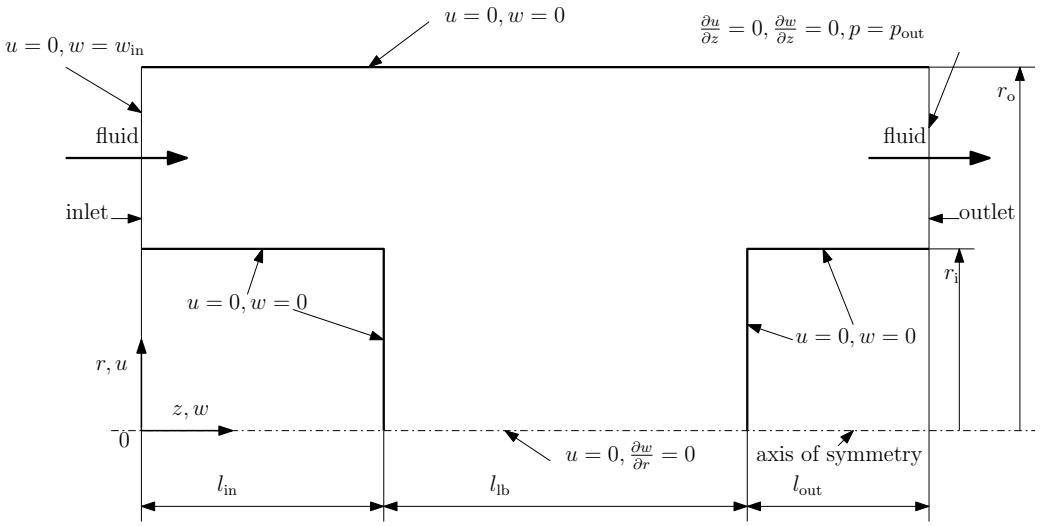

Figure 3.1: Computational domain and boundary conditions for the 2D axisymmetric one phase flow.

has been re-written to replace the 2D conservation equations in Cartesian form by the corresponding 2D axisymmetric ones

$$\frac{1}{r}\frac{\partial ru^2}{\partial r} + \frac{\partial uw}{\partial z} = -\frac{\partial p}{\partial r} + \frac{1}{\mathrm{Re}}\left[\frac{1}{r}\frac{\partial}{\partial r}\left(r\frac{\partial u}{\partial r}\right) + \frac{\partial^2 u}{\partial z^2} - \frac{u}{r^2}\right], \tag{3.1a}$$

$$\frac{1}{r}\frac{\partial ruw}{\partial r} + \frac{\partial w^2}{\partial z} = -\frac{\partial p}{\partial z} + \frac{1}{\mathrm{Re}}\left[\frac{1}{r}\frac{\partial}{\partial r}\left(r\frac{\partial w}{\partial r}\right) + \frac{\partial^2 w}{\partial z^2}\right], \tag{3.1b}$$

$$\frac{1}{r}\frac{\partial ru}{\partial r} + \frac{\partial w}{\partial z} = 0, \tag{3.1c}$$

which are in strong conservative and dimensionless form. In addition the computational domain was changed from a rectangular shape to the cylindrical geometry depicted in fig. 3.1 which is required for the EMA project.

The conservation equations were made dimensionless using the scales $r_{\text{o}}^* - r_{\text{i}}^*$, w_{in}^*, and $\rho_{\text{fluid}} \cdot w_{\text{in}}^{*2}$ for lengths, velocity, and pressure, respectively. The Reynolds number is defined as

$$\mathrm{Re} = \frac{w_{\text{in}}^* \left(r_{\text{o}}^* - r_{\text{i}}^*\right)}{\nu_{\text{fluid}}}. \tag{3.2}$$

To solve the flow problem a finite volume method on a staggered grid (uniform or nonuniform) is used. The convective terms were discretized using a central scheme and the variables were linearly interpolated. Along the cell edges the variables and derivatives were treated as constants. The solution vector of the nonlinear problem is calculated by Picard iteration (outer iterations) and using the MATLAB-operator `mldivide` (inner iterations) for solving the linearized discretized conservation equations.

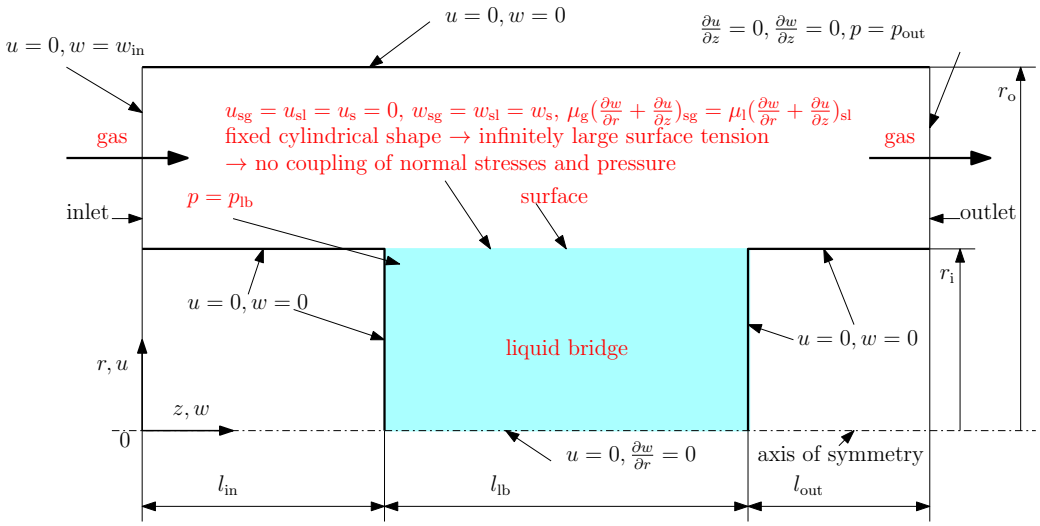

Figure 3.2: Computational domain and boundary conditions for the 2D axisymmetric two phase flow.

In a second step a second fluid phase was introduced. This enabled the definition of a liquid bridge surrounded by the second (gas) phase. The new boundary conditions and the domain of the liquid bridge are depicted in fig. 3.2 (in red: modification of the previous step).

In that model there is no coupling of normal stresses and pressure between the liquid bridge and the gas phase due to the assumption of infinitely large surface tension of the liquid. Hence, the pressure has to be fixed at some point in the domain of the liquid bridge.

The conservation equations for the liquid bridge are as follows

$$\frac{1}{r}\frac{\partial r u^2}{\partial r} + \frac{\partial u w}{\partial z} = -\frac{\rho_{\text{g}}}{\rho_{\text{l}}}\frac{\partial p}{\partial r} + \frac{\nu_{\text{l}}}{\nu_{\text{g}}}\frac{1}{\text{Re}}\left[\frac{1}{r}\frac{\partial}{\partial r}\left(r\frac{\partial u}{\partial r}\right) + \frac{\partial^2 u}{\partial z^2} - \frac{u}{r^2}\right], \tag{3.3a}$$

$$\frac{1}{r}\frac{\partial r u w}{\partial r} + \frac{\partial w^2}{\partial z} = -\frac{\rho_{\text{g}}}{\rho_{\text{l}}}\frac{\partial p}{\partial z} + \frac{\nu_{\text{l}}}{\nu_{\text{g}}}\frac{1}{\text{Re}}\left[\frac{1}{r}\frac{\partial}{\partial r}\left(r\frac{\partial w}{\partial r}\right) + \frac{\partial^2 w}{\partial z^2}\right], \tag{3.3b}$$

$$\frac{1}{r}\frac{\partial r u}{\partial r} + \frac{\partial w}{\partial z} = 0. \tag{3.3c}$$

This set of discretized equations is solved by the same method as for the single-phase problem before.

In a third step the thermocapillary flow is treated. To that end, the conservation equation for the thermal energy, cf. (3.6b) and (3.7b), as well as new boundary conditions, cf. fig. 3.3 (in red: changes to the previous step), are introduced.

The equations were non-dimensionalized by using the scales l^*_{lb}, $\gamma_{\text{l}}\Delta T/\rho_{\text{l}}\nu_{\text{l}}$, $\gamma_{\text{l}}\Delta T/l^*_{\text{lb}}$, and $\Delta T = T_{\text{hot}} - T_{\text{cold}}$ for length, velocity, pressure, and temperature, respectively.

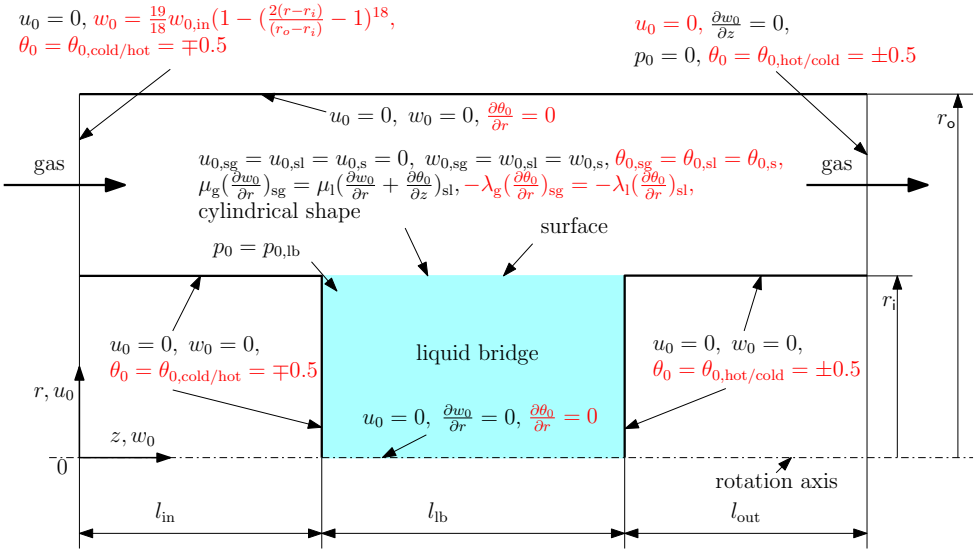

Figure 3.3: Computational domain and boundary conditions for the 2D axisymmetric thermocapillary flow.

A normalized temperature

$$\theta = \frac{T - (T_\mathrm{hot} + T_\mathrm{cold})/2}{\Delta T} \tag{3.4}$$

is introduced and the Reynolds number is defined as

$$\mathrm{Re} = \frac{\gamma_\mathrm{l} \Delta T l^*_\mathrm{lb}}{\rho_\mathrm{l} \nu_\mathrm{l}^2}. \tag{3.5}$$

The Prandtl number is $\mathrm{Pr} = \nu_\mathrm{l}/\kappa_\mathrm{l}$. The conservation equations to be solved for the liquid phase are

$$\mathrm{Re}\, \nabla \cdot (\boldsymbol{u_0 u_0}) = -\nabla p_0 + \Delta \boldsymbol{u_0}, \tag{3.6a}$$

$$\mathrm{Re}\, \nabla \cdot (\boldsymbol{u_0} \theta_0) = \frac{1}{\mathrm{Pr}} \Delta \theta_0, \tag{3.6b}$$

$$\nabla \cdot \boldsymbol{u_0} = 0. \tag{3.6c}$$

For the gas phase we solve

$$\mathrm{Re}\, \nabla \cdot (\boldsymbol{u_0 u_0}) = -\frac{\rho_\mathrm{l}}{\rho_\mathrm{g}} \nabla p_0 + \frac{\nu_\mathrm{g}}{\nu_\mathrm{l}} \Delta \boldsymbol{u_0}, \tag{3.7a}$$

$$\mathrm{Re}\, \nabla \cdot (\boldsymbol{u_0} \theta_0) = \frac{\kappa_\mathrm{g}}{\kappa_\mathrm{l}} \frac{1}{\mathrm{Pr}} \Delta \theta_0, \tag{3.7b}$$

$$\nabla \cdot \boldsymbol{u_0} = 0. \tag{3.7c}$$

Since the Picard iteration converges only slowly, we have now implemented Newton's method for the outer iterations.

In the fourth step the code for the linear stability of the obtained solution (basic state) was developed. For the linear stability analysis of the basic state the 3D unsteady conservation equations are considered. The conservation equations for the liquid phase

$$\partial_t \boldsymbol{U} + \mathrm{Re}\,\nabla\cdot(\boldsymbol{U}\boldsymbol{U}) = -\nabla P + \Delta\boldsymbol{U}, \tag{3.8a}$$

$$\partial_t \Theta + \mathrm{Re}\,\nabla\cdot(\boldsymbol{U}\Theta) = \frac{1}{\mathrm{Pr}}\Delta\Theta, \tag{3.8b}$$

$$\nabla\cdot\boldsymbol{U} = 0, \tag{3.8c}$$

and for the gas phase

$$\partial_t \boldsymbol{U} + \mathrm{Re}\,\nabla\cdot(\boldsymbol{U}\boldsymbol{U}) = -\frac{\rho_\mathrm{l}}{\rho_\mathrm{g}}\nabla P + \frac{\nu_\mathrm{g}}{\nu_\mathrm{l}}\Delta\boldsymbol{U}, \tag{3.9a}$$

$$\partial_t \Theta + \mathrm{Re}\,\nabla\cdot(\boldsymbol{U}\Theta) = \frac{\kappa_\mathrm{g}}{\kappa_\mathrm{l}}\frac{1}{\mathrm{Pr}}\Delta\Theta, \tag{3.9b}$$

$$\nabla\cdot\boldsymbol{U} = 0, \tag{3.9c}$$

are written in strong conservative form. The time was non-dimensionalized by the scale ${l^*_\mathrm{lb}}^2/\nu_\mathrm{l}$. The variables of the total flow in (3.8a) to (3.9c) are decomposed and replaced by variables of the basic state and perturbations:

$$\boldsymbol{U} = \boldsymbol{u_0} + \boldsymbol{u}, \tag{3.10a}$$

$$P = p_0 + p, \tag{3.10b}$$

$$\Theta = \theta_0 + \theta. \tag{3.10c}$$

$$\tag{3.10d}$$

A linearization with respect to infinitely small perturbations u, v, w, p, θ results in the following equations for the gas phase,

$$\frac{\partial u}{\partial t} + \mathrm{Re}\left[\left(\frac{1}{r}+\frac{\partial}{\partial r}\right)(2u_0 u) + \frac{1}{r}\frac{\partial u_0 v}{\partial\varphi} + \frac{\partial\left(u_0 w + u w_0\right)}{\partial z}\right] = \\ = -\frac{\rho_\mathrm{l}}{\rho_\mathrm{g}}\frac{\partial p}{\partial r} + \frac{\nu_\mathrm{g}}{\nu_\mathrm{l}}\left[\frac{1}{r}\frac{\partial}{\partial r}\left(r\frac{\partial u}{\partial r}\right) - \frac{u}{r^2} + \frac{1}{r^2}\frac{\partial^2 u}{\partial\varphi^2} - \frac{2}{r^2}\frac{\partial v}{\partial\varphi} + \frac{\partial^2 u}{\partial z^2}\right], \tag{3.11a}$$

$$\frac{\partial v}{\partial t} + \mathrm{Re}\left[\left(\frac{2}{r}+\frac{\partial}{\partial r}\right) v u_0 + \frac{\partial v w_0}{\partial z}\right] = \\ = -\frac{\rho_\mathrm{l}}{\rho_\mathrm{g}}\frac{1}{r}\frac{\partial p}{\partial\varphi} + \frac{\nu_\mathrm{g}}{\nu_\mathrm{l}}\left[\frac{1}{r}\frac{\partial}{\partial r}\left(r\frac{\partial v}{\partial r}\right) - \frac{v}{r^2} + \frac{2}{r^2}\frac{\partial u}{\partial\varphi} + \frac{1}{r^2}\frac{\partial^2 v}{\partial\varphi^2} + \frac{\partial^2 v}{\partial z^2}\right], \tag{3.11b}$$

$$\frac{\partial w}{\partial t} + \mathrm{Re}\left[\left(\frac{1}{r}+\frac{\partial}{\partial r}\right)(w_0 u + w u_0) + \frac{1}{r}\frac{\partial w_0 v}{\partial\varphi} + \frac{\partial\left(2 w_0 w\right)}{\partial z}\right] = \\ = -\frac{\rho_\mathrm{l}}{\rho_\mathrm{g}}\frac{\partial p}{\partial z} + \frac{\nu_\mathrm{g}}{\nu_\mathrm{l}}\left[\frac{1}{r}\frac{\partial}{\partial r}\left(r\frac{\partial w}{\partial r}\right) + \frac{1}{r^2}\frac{\partial^2 w}{\partial\varphi^2} + \frac{\partial^2 w}{\partial z^2}\right], \tag{3.11c}$$

$$\frac{\partial\theta}{\partial t}+\mathrm{Re}\left[\left(\frac{1}{r}+\frac{\partial}{\partial r}\right)(\theta_0 u+\theta u_0)+\frac{1}{r}\frac{\partial\theta_0 v}{\partial\varphi}+\frac{\partial\left(\theta_0 w+\theta w_0\right)}{\partial z}\right]= \\ =\frac{\kappa_\mathrm{g}}{\kappa_\mathrm{l}}\frac{1}{\mathrm{Pr}}\left[\frac{1}{r}\frac{\partial}{\partial r}\left(r\frac{\partial\theta}{\partial r}\right)+\frac{1}{r^2}\frac{\partial^2\theta}{\partial\varphi^2}+\frac{\partial^2\theta}{\partial z^2}\right], \quad (3.11\mathrm{d})$$

$$\frac{1}{r}\frac{\partial ru}{\partial r}+\frac{1}{r}\frac{\partial v}{\partial\varphi}+\frac{\partial w}{\partial z}=0. \quad (3.11\mathrm{e})$$

These linear equations can be solved by the normal-mode ansatz

$$[u,v,w,p,\theta]=\left[\hat{u},\hat{v},\hat{w},\hat{p},\hat{\theta}\right](r,z)\,\mathrm{e}^{\gamma t+\mathrm{i}m\varphi}+\mathrm{c.c.}, \quad (3.12)$$

where γ denotes the complex growth rate and m the azimuthal wave number. Inserting this ansatz into the linear perturbation equations one obtains linear differential equations for the amplitudes $\hat{u}$, $\hat{v}$, $\hat{w}$, $\hat{p}$, $\hat{\theta}$ which merely depend on r and z,

$$\gamma\hat{u}+\mathrm{Re}\left[\left(\frac{1}{r}+\frac{\partial}{\partial r}\right)(2u_0\hat{u})+\frac{u_0\mathrm{i}\hat{v}m}{r}+\frac{\partial\left(u_0\hat{w}+\hat{u}w_0\right)}{\partial z}\right]= \\ =-\frac{\rho_\mathrm{l}}{\rho_\mathrm{g}}\frac{\partial\hat{p}}{\partial r}+\frac{\nu_\mathrm{g}}{\nu_\mathrm{l}}\left[\frac{1}{r}\frac{\partial}{\partial r}\left(r\frac{\partial\hat{u}}{\partial r}\right)-\left(m^2+1\right)\frac{\hat{u}}{r^2}-\frac{2}{r^2}\mathrm{i}\hat{v}m+\frac{\partial^2\hat{u}}{\partial z^2}\right] \quad (3.13\mathrm{a})$$

$$\gamma\mathrm{i}\hat{v}+\mathrm{Re}\left[\left(\frac{2}{r}+\frac{\partial}{\partial r}\right)\mathrm{i}\hat{v}u_0+\frac{\partial\mathrm{i}\hat{v}w_0}{\partial z}\right]= \\ =+\frac{\rho_\mathrm{l}}{\rho_\mathrm{g}}\frac{1}{r}\hat{p}m+\frac{\nu_\mathrm{g}}{\nu_\mathrm{l}}\left[-\frac{2}{r^2}\hat{u}m+\frac{1}{r}\frac{\partial}{\partial r}\left(r\frac{\partial\mathrm{i}\hat{v}}{\partial r}\right)-\left(m^2+1\right)\frac{\mathrm{i}\hat{v}}{r^2}+\frac{\partial^2\mathrm{i}\hat{v}}{\partial z^2}\right] \quad (3.13\mathrm{b})$$

$$\gamma\hat{w}+\mathrm{Re}\left(\frac{1}{r}\frac{\partial r\left(w_0\hat{u}+\hat{w}u_0\right)}{\partial r}+\frac{w_0\mathrm{i}\hat{v}m}{r}+\frac{\partial\left(2w_0\hat{w}\right)}{\partial z}\right)= \\ =-\frac{\rho_\mathrm{l}}{\rho_\mathrm{g}}\frac{\partial\hat{p}}{\partial z}+\frac{\nu_\mathrm{g}}{\nu_\mathrm{l}}\left[\frac{1}{r}\frac{\partial}{\partial r}\left(r\frac{\partial\hat{w}}{\partial r}\right)-m^2\frac{\hat{w}}{r^2}+\frac{\partial^2\hat{w}}{\partial z^2}\right] \quad (3.13\mathrm{c})$$

$$\gamma\hat{\theta}+\mathrm{Re}\left[\frac{1}{r}\frac{\partial r\left(\theta_0\hat{u}+\hat{\theta}u_0\right)}{\partial r}+\frac{\theta_0\mathrm{i}\hat{v}m}{r}+\frac{\partial\left(\theta_0\hat{w}+\hat{\theta}w_0\right)}{\partial z}\right]= \\ =\frac{\kappa_\mathrm{g}}{\kappa_\mathrm{l}}\frac{1}{\mathrm{Pr}}\left[\frac{1}{r}\frac{\partial}{\partial r}\left(r\frac{\partial\hat{\theta}}{\partial r}\right)-m^2\frac{\hat{\theta}}{r^2}+\frac{\partial^2\hat{\theta}}{\partial z^2}\right] \quad (3.13\mathrm{d})$$

$$\frac{1}{r}\frac{\partial r\hat{u}}{\partial r}+\frac{1}{r}\mathrm{i}\hat{v}m+\frac{\partial\hat{w}}{\partial z}=0. \quad (3.13\mathrm{e})$$

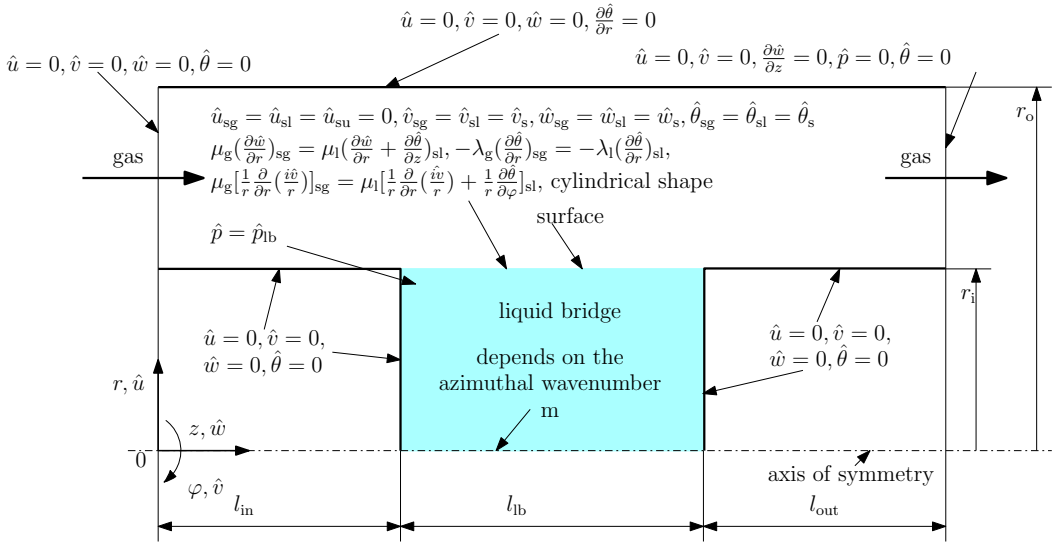

Figure 3.4: Computational domain and boundary conditions for the linear stability analysis.

Table 3.1: Boundary conditions on the axis of symmetry.

$m=0$	$\hat{u}=0$	$\hat{v}=0$	$\partial_r\hat{w}=0$	$\partial_r\hat{\theta}=0$
$m=1$	$\partial_r\hat{u}=0$	$\partial_r\hat{v}=0$	$\hat{w}=0$	$\hat{\theta}=0$
$m>1$	$\hat{u}=0$	$\hat{v}=0$	$\hat{w}=0$	$\hat{\theta}=0$

For the liquid phase the ratios ρ_l/ρ_g, ν_g/ν_l and κ_g/κ_l in (3.11a) through (3.11e) and (3.13a) through (3.13e) are replaced by 1. Defining the boundary conditions and discretizing the equations this results in a generalized eigenvalue problem

$$\mathsf{A}\cdot\boldsymbol{x}=-\gamma\mathsf{B}\cdot\boldsymbol{x}. \tag{3.14}$$

Here the same discretization scheme as for the basic state was applied. The complex growth rate represents the eigenvalue γ and the perturbation amplitudes the eigenvector $\boldsymbol{x}$. Matrices A and B represent coefficients of the set of algebraic equations. Because of the assumed incompressibility of the fluids matrix B is singular. To save main memory for the later explained solution method the transformation $i\hat{v}=v^*$ to obtain pure real matrices A and B is done . The boundary conditions are shown in fig. 3.4. Boundary conditions for the axis of symmetry are dependent on the azimuthal wave number m and are shown in table 3.1. Those conditions can be derived from the uniqueness conditions $\partial\boldsymbol{u}/\partial\varphi=0$ and $\partial\theta/\partial\varphi=0$ on $r=0$. For the discretized algebraic set of equations as many solutions as dependent variables N exist. So the degrees of freedom were reduced from infinity for the continuous system to N for the discrete system. But just one solution has to be found. It is the

mode n with the largest real part of the growth rate ($\max_n \Re(\gamma_n)$) and called most dangerous mode. It can be found with the strategy of (Meerbergen *et al.*, 1994). In a first step 12 eigenvalues with the smallest magnitude are calculated. An Implicitly Restarted Arnoldi Method which is implemented in ARPACK (Lehoucq *et al.*, 1998) and used by MATLAB with the `eigs` command is therefore applied. The necessary shift invert transformation

$$\mathsf{B} \cdot \boldsymbol{x} = \frac{1}{-\gamma} \mathsf{A} \cdot \boldsymbol{x} \tag{3.15}$$

is done by `eigs`. The second step is a validation step where 5 eigenvalues with the largest magnitude of the Cayley transformation

$$(\mathsf{A} - \alpha_2 \mathsf{B}) \cdot \boldsymbol{x} = \frac{-\gamma - \alpha_2}{-\gamma - \alpha_1} (\mathbf{A} - \alpha_1 \mathbf{B}) \cdot \boldsymbol{x} \tag{3.16}$$

are calculated. The most dangerous mode can be found among those 17 solutions of the eigenvalue problem. For the calculation of α_1 and α_2 the parameters $r = 5$ and $\rho_{\text{user}} = 1.1$ are chosen (see Meerbergen *et al.*, 1994). The Cayley transformation has to be programmed whereas the shift invert transformation is again done by `eigs`.

A mode is linearly stable if $\Re(\gamma_n) < 0$, linearly unstable if $\Re(\gamma_n) > 0$ and neutrally stable if $\Re(\gamma_n) = 0$. It is steady if $\Im(\gamma_n) = 0$ and oscillating if $\Im(\gamma_n) \neq 0$. If the most dangerous mode is neutrally stable it is called neutral mode. To find such a neutral mode control parameters like Re are increased or decreased e.g. 5 % until the sign of $\max_n \Re(\gamma_n)$ changes which means that at least one root exists within the interval of the control parameter. Such a root and, hence, the neutral mode can be efficiently found with the strategy of (Gottlieb, 2010). It is a kind of combination of regula falsi and bisection.

Neutral modes of a basic state can be found for different azimuthal wave numbers m. Because of the rotational symmetry of the liquid bridge m can only be a natural number ($m \in \mathbb{N}$) and determines the azimuthal periodicity of the mode. At the smallest control parameter where a neutral mode exists the basic flow becomes linearly unstable which means the steady 2D axisymmetric flow changes to unsteady or 3D (or both). The mode and the control parameter are then called critical. Note that with further increasing of the control parameter again a critical mode can be found. That means that the flow becomes linearly stable again. So different neutral modes have to be calculated to find the critical one and therefore the stability boundary.

To evaluate the energy conservation of the solutions obtained and to identify the instability mechanisms of the critical modes an *a posteriori* energy analysis was applied. This method is widely known and the equations are derived for example in Wanschura *et al.* (1995) for a liquid bridge where the ambient gas is neglected. The scalar product of the linearized momentum equations (3.11a)–(3.11c) with the perturbation velocity vector $\boldsymbol{u}$ and integration over the gas volume gives the rate of change of the the kinetic energy $\mathrm{d}E_{\text{kin}}/\mathrm{d}t$ in the gas. The procedure for the liquid

is similar. By splitting the resulting equations in volume and surface integrals the following balance can be made for the gas and the liquid phase:

$$\frac{\mathrm{d}E_{\mathrm{kin,g}}}{\mathrm{d}t} = \frac{1}{2}\int_{\mathcal{V}_\mathrm{g}} \frac{\partial \boldsymbol{u}^2}{\partial t}\partial\mathcal{V}_\mathrm{g} = -D_\mathrm{g} + M_{\varphi,\mathrm{g}} + M_{z,\mathrm{g}} + \sum_{i=1}^{5} I_{\mathrm{vi,g}} + K_\mathrm{g} \tag{3.17a}$$

$$\frac{\mathrm{d}E_{\mathrm{kin,l}}}{\mathrm{d}t} = \frac{1}{2}\int_{\mathcal{V}_\mathrm{l}} \frac{\partial \boldsymbol{u}^2}{\partial t}\partial\mathcal{V}_\mathrm{l} = -D_\mathrm{l} + M_{\varphi,\mathrm{l}} + M_{z,\mathrm{l}} + \sum_{i=1}^{5} I_{\mathrm{vi,l}}. \tag{3.17b}$$

The viscous dissipation in the gas is obtained with the relation

$$\begin{aligned} D_\mathrm{g} = \frac{\nu_\mathrm{g}}{\nu_\mathrm{l}}\int_{\mathcal{V}_\mathrm{g}} \Bigg[&\left(\frac{\partial u}{\partial r}\right)^2 + \left(\frac{1}{r}\frac{\partial u}{\partial \varphi} - \frac{v}{r}\right)^2 + \left(\frac{\partial u}{\partial z}\right)^2 + \\ &+ \left(\frac{\partial v}{\partial r}\right)^2 + \left(\frac{1}{r}\frac{\partial v}{\partial \varphi} + \frac{u}{r}\right)^2 + \left(\frac{\partial v}{\partial z}\right)^2 + \\ &+ \left(\frac{\partial w}{\partial r}\right)^2 + \left(\frac{1}{r}\frac{\partial w}{\partial \varphi}\right)^2 + \left(\frac{\partial w}{\partial z}\right)^2 \Bigg] \partial\mathcal{V}_\mathrm{g} + \\ &+ \frac{\nu_\mathrm{g}}{\nu_\mathrm{l}}\int_{\mathcal{S}_\mathrm{s}} \frac{v^2}{r}\partial\mathcal{S}_\mathrm{s}, \end{aligned} \tag{3.18}$$

where $\mathcal{V}_\mathrm{g}$ denotes the gas volume and $\mathcal{S}_\mathrm{s}$ the free surface of the liquid bridge. For the liquid bridge the factor $\nu_\mathrm{g}/\nu_\mathrm{l}$ of the volume integral is replaced by 1 and by -1 for the surface integral. The integration domain is then of course the volume of the liquid bridge $\mathcal{V}_\mathrm{l}$. The work done per time by thermocapillary shear forces for the gas are

$$M_{\varphi,\mathrm{g}} = -\frac{\nu_\mathrm{g}}{\nu_\mathrm{l}}\int_{\mathcal{S}_\mathrm{s}} \left(v\frac{\partial v}{\partial r} - \frac{v^2}{r}\right)\partial\mathcal{S}_\mathrm{s}, \tag{3.19}$$

in azimuthal direction and

$$M_{z,\mathrm{g}} = -\frac{\nu_\mathrm{g}}{\nu_\mathrm{l}}\int_{\mathcal{S}_\mathrm{s}} w\frac{\partial w}{\partial r}\partial\mathcal{S}_\mathrm{s} \tag{3.20}$$

in axial direction. For the liquid $-\nu_\mathrm{g}/\nu_\mathrm{l}$ is replaced by 1. The transfer rate of kinetic energy from the basic state to the perturbed mode in the gas consists of five terms:

$$I_{\mathrm{v,g}} = \sum_{i=1}^{5} I_{\mathrm{vi,g}} = -\mathrm{Re}\int_{\mathcal{V}_\mathrm{g}} \left(v^2\frac{u_0}{r} + u^2\frac{\partial u_0}{\partial r} + wu\frac{\partial u_0}{\partial z} + wu\frac{\partial w_0}{\partial r} + w^2\frac{\partial w_0}{\partial z}\right)\partial\mathcal{V}_\mathrm{g} \tag{3.21}$$

For the liquid bridge those terms remain the same but the integration domain changes to $\mathcal{V}_\mathrm{l}$. The transport of kinetic energy out of the gas domain

$$K_\mathrm{g} = -\frac{1}{2}\mathrm{Re}\int_{\mathcal{S}_\mathrm{out}} w_0 w^2 \partial\mathcal{S}_\mathrm{out} \tag{3.22}$$

is also needed. The normalized residuals of the kinetic energy are determined as follows:

$$\delta e_{\mathrm{kin,g}} = \frac{|-\partial_t E_{\mathrm{kin,g}} - D_{\mathrm{g}} + M_{\varphi,\mathrm{g}} + M_{z,\mathrm{g}} + I_{\mathrm{v,g}} + K_{\mathrm{g}}|}{\max\left\{|\partial_t E_{\mathrm{kin,g}}|, |D_{\mathrm{g}}|, |M_{\varphi,\mathrm{g}}|, |M_{z,\mathrm{g}}|, |I_{\mathrm{v1,g}}|, \ldots, |I_{\mathrm{v5,g}}|, |K_{\mathrm{g}}|\right\}}, \tag{3.23a}$$

$$\delta e_{\mathrm{kin,l}} = \frac{|-\partial_t E_{\mathrm{kin,l}} - D_{\mathrm{l}} + M_{\varphi,\mathrm{l}} + M_{z,\mathrm{l}} + I_{\mathrm{v,l}}|}{\max\left\{|\partial_t E_{\mathrm{kin,l}}|, |D_{\mathrm{l}}|, |M_{\varphi,\mathrm{l}}|, |M_{z,\mathrm{l}}|, |I_{\mathrm{v1,l}}|, \ldots, |I_{\mathrm{v5,l}}|\right\}}. \tag{3.23b}$$

To identify thermal energy transfer between basic state and the perturbation mode in the ambient gas the equation for the thermal energy (3.11d) is multiplied with the perturbation temperature θ and integrated over the gas volume. In the following it will be called thermal energy balance although $E_{\mathrm{T,g}}$ is no energy as defined in thermodynamics. The procedure for the liquid is similar. By splitting the resulting equations in volume and surface integrals the following balance can be made for the gas and the liquid phase

$$\partial_t E_{\mathrm{T,g}} = \frac{1}{2}\int_{\mathcal{V}_{\mathrm{g}}} \frac{\partial\theta^2}{\partial t}\partial\mathcal{V}_{\mathrm{g}} = -D_{\mathrm{T,g}} - H_{\mathrm{g}} + \sum_{i=1}^{2} I_{\mathrm{Ti,g}}, \tag{3.24a}$$

$$\partial_t E_{\mathrm{T,l}} = \frac{1}{2}\int_{\mathcal{V}_{\mathrm{l}}} \frac{\partial\theta^2}{\partial t}\partial\mathcal{V}_{\mathrm{l}} = -D_{\mathrm{T,l}} - H_{\mathrm{l}} + \sum_{i=1}^{2} I_{\mathrm{Ti,l}}. \tag{3.24b}$$

The terms for the ambient gas are calculated with the following relations

$$D_{T,\mathrm{g}} = \frac{\kappa_{\mathrm{g}}}{\kappa_{\mathrm{l}}}\frac{1}{\mathrm{Pr}}\int_{\mathcal{V}_{\mathrm{g}}}\left[\left(\frac{\partial\theta}{\partial r}\right)^2 + \left(\frac{1}{r}\frac{\partial\theta}{\partial\varphi}\right)^2 + \left(\frac{\partial\theta}{\partial z}\right)^2\right]\partial\mathcal{V}_{\mathrm{g}}, \tag{3.25a}$$

$$H_{\mathrm{g}} = \frac{\kappa_{\mathrm{g}}}{\kappa_{\mathrm{l}}}\frac{1}{\mathrm{Pr}}\int_{\mathcal{S}_{\mathrm{s}}} \theta\frac{\partial\theta}{\partial r}\partial\mathcal{S}_{\mathrm{s}}, \tag{3.25b}$$

$$I_{\mathrm{T,g}} = \sum_{i=1}^{2} I_{\mathrm{Ti,g}} = -\mathrm{Re}\int_{\mathcal{V}_{\mathrm{g}}} \theta\left(u\frac{\partial\theta_0}{\partial r} + w\frac{\partial\theta_0}{\partial z}\right)\partial\mathcal{V}_{\mathrm{g}}. \tag{3.25c}$$

For the liquid bridge $\kappa_{\mathrm{g}}/\kappa_{\mathrm{l}}$ is replaced by 1 in (3.25a) and by -1 in (3.25b). The integration domain in (3.25a) and (3.25c) changes of course to $\mathcal{V}_{\mathrm{l}}$. The normalized residuals of the thermal energy are determined as follows

$$\delta e_{\mathrm{T,g}} = \frac{|-\partial_t E_{\mathrm{T,g}} - D_{\mathrm{T,g}} - H_{\mathrm{g}} + I_{\mathrm{T,g}}|}{\max\left\{|\partial_t E_{\mathrm{T,g}}|, |D_{\mathrm{T,g}}|, |H_{\mathrm{g}}|, |I_{\mathrm{T1,g}}|, |I_{\mathrm{T2,g}}|\right\}}, \tag{3.26a}$$

$$\delta e_{\mathrm{T,l}} = \frac{|-\partial_t E_{\mathrm{T,l}} - D_{\mathrm{T,l}} - H_{\mathrm{l}} + I_{\mathrm{T,l}}|}{\max\left\{|\partial_t E_{\mathrm{T,l}}|, |D_{\mathrm{T,l}}|, |H_{\mathrm{l}}|, |I_{\mathrm{T1,l}}|, |I_{\mathrm{T2,l}}|\right\}}. \tag{3.26b}$$

The program to solve for the basic state, carry out the linear stability analysis and perform the a posteriori energy analysis was developed in MATLAB and is called `MaranStable`.

The work in this package is completed.

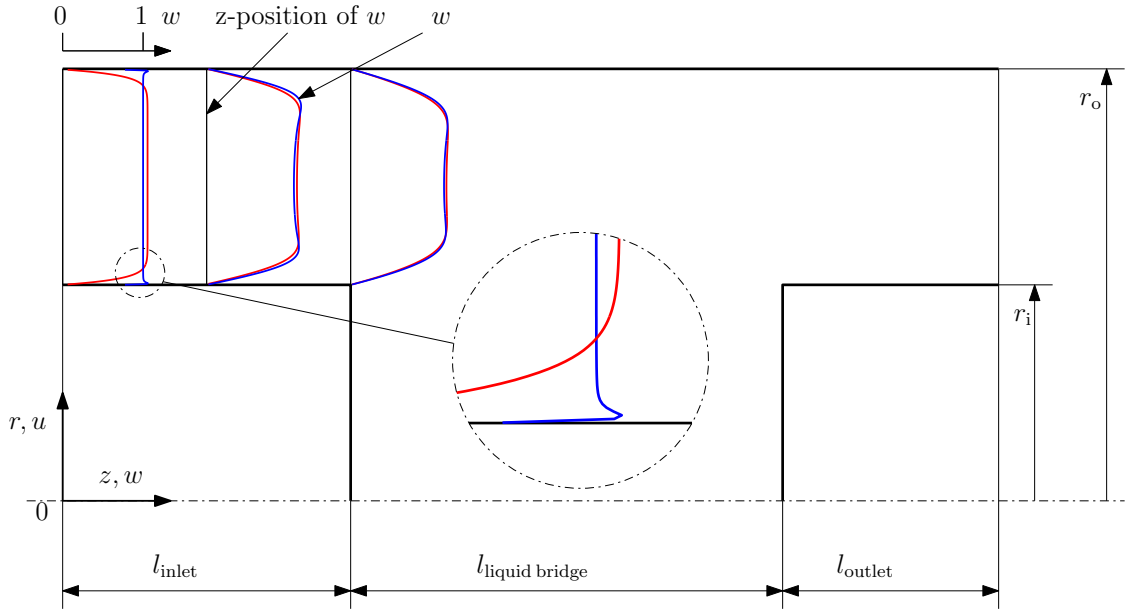

Figure 3.5: Development of the flow for a constant (blue) and a regularized (red) inlet velocity profile for Re = 300.

WP B2.2: Validation of the CG-code

For first checks the velocity profile which develops in the gas downstream from the inlet profile (calculated numerically) was compared with the fully developed flow for which a closed-form analytical solution is available. For this simulations the dimensions of geometry, the inlet velocity (profile), the Reynolds number, and the grid structure (uniform/nonuniform) were varied.

We find that the flow develops to the analytical solution sufficiently far downstream. However, the flow immediately behind the inlet exhibits some peculiarities which have not been recognized by a number of previous numerical investigators using coarse grids. The velocity profiles are depicted in fig. 3.5. Thin black lines indicate the location at which the velocity profiles (in color) are evaluated. A constant inlet velocity represents a singular boundary condition, because the velocity on the rigid walls must be zero. Slightly downstream from the inlet the initial velocity jump causes a peak in the near-wall region. This can be seen in the zoom provided in the inset figure. The velocity profiles exhibits a weak minimum at approximately $(r_o + r_i)/2$. This location is independent of the specific inlet velocity profile (singular or regularized). The reason for the observed velocity overshoot is the deceleration of the fluid in the immediate vicinity of the wall (Darbandi & Schneider, 1998). Quite a fine grid is needed to resolve this behavior.

We employed different methods to verify the code. One possibility is to set the axial velocity $w = 1$ and the radial velocity $u = 0$ on all boundaries, as in (Muldoon, 2004). The computations should then yield the same velocity $w = 1$ in the whole computational domain. Another test makes use of dedicated artificial solutions

(Muldoon, 2004). If one assumes a solution in simple polynomial form

$$u = r, \tag{3.27a}$$
$$w = z, \tag{3.27b}$$
$$p = rz, \tag{3.27c}$$

and inserts this ansatz into the governing equations (3.1a)–(3.1c), then one can analytically calculate the required source terms U, W, C such that the equations are satisfied. One thus arrives at

$$\frac{1}{r}\frac{\partial r r^2}{\partial r} + \frac{\partial r z}{\partial z} = -\frac{\partial r z}{\partial r} + \frac{1}{\mathrm{Re}}\left[\frac{1}{r}\frac{\partial}{\partial r}\left(r\frac{\partial r}{\partial r}\right) + \frac{\partial^2 r}{\partial z^2} - \frac{r}{r^2}\right] + U, \tag{3.28a}$$
$$U = 3r + r + z - \frac{1}{\mathrm{Re}}\left[\frac{1}{r} + 0 - \frac{1}{r}\right] = 4r + z, \tag{3.28b}$$
$$\frac{1}{r}\frac{\partial r r z}{\partial r} + \frac{\partial z^2}{\partial z} = -\frac{\partial r z}{\partial z} + \frac{1}{\mathrm{Re}}\left[\frac{1}{r}\frac{\partial}{\partial r}\left(r\frac{\partial z}{\partial r}\right) + \frac{\partial^2 z}{\partial z^2}\right] + W, \tag{3.28c}$$
$$W = 2z + 2z + r - \frac{1}{\mathrm{Re}}\left[0 + 0\right] = 4z + r, \tag{3.28d}$$
$$\frac{1}{r}\frac{\partial r r}{\partial r} + \frac{\partial z}{\partial z} = 0 + C, \tag{3.28e}$$
$$C = 2 + 1 = 3. \tag{3.28f}$$

After introducing these source terms into the discretized set of equations and using the proper (polynomial) boundary conditions the result of the simulation should reproduce the polynomial flow field within machine precision.

>From the above test we could conclude that the discretization scheme is of second order for w (axial direction) and ru (radial direction). In addition, we found that the use of $\partial_r u^2 + u^2/r$ instead of $r^{-1}\partial_r r u^2$ (which is not of second order for ru) in the radial momentum equation is more accurate.

In addition to these general tests, the code for the 2D steady thermocapillary flow was verified by comparing the computed flow and temperature fields with published numerical results (Kuhlmann, 1999). Since the models available in the literature do not include the effect of the surrounding gas phase, the ratios of the dynamic viscosities $\mu_\mathrm{l}/\mu_\mathrm{g}$ and heat conductivities $\lambda_\mathrm{l}/\lambda_\mathrm{g}$ were set to 10^{10} to practically eliminate the influence of the gas phase on the thermocapillary flow in the liquid. An example for such a benchmark calculation with a high grid resolution is provided in fig. 3.6.

As for the basic state a verification of the linear stability part of the CG-code is not possible at the time being because of the unavailability of suitable published work. To verify at least the C-code of `MaranStable` computed stability boundaries dependent on Pr were compared with results of (Levenstam *et al.*, 2001). Since they neglected the gas phase in their model and assumed an adiabatic surface we also had to reduce our model for that test to a single-phase flow (C-model). The relative error of the critical Reynolds number Re_c was related to the results of (Levenstam

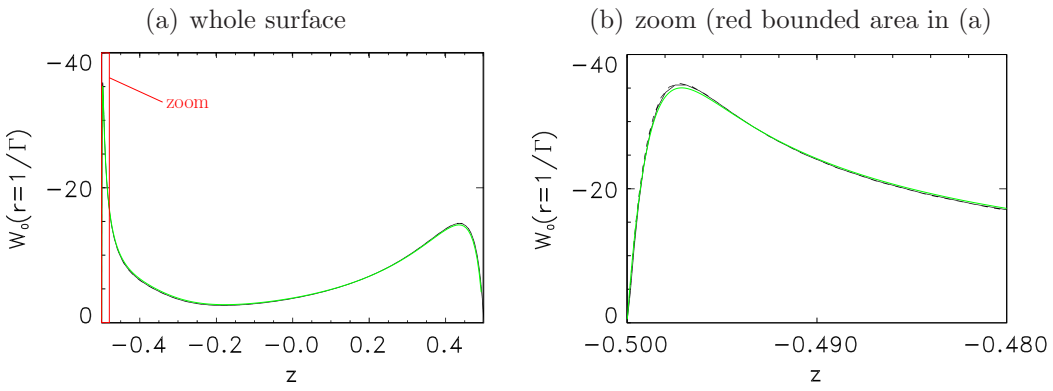

Figure 3.6: Axial surface velocity w_0 in units of ν_1/l^*_{lb} along the surface z (in green: own results, in black: (Kuhlmann *et al.*, 2000)) for Re = 412 and Pr = 35.

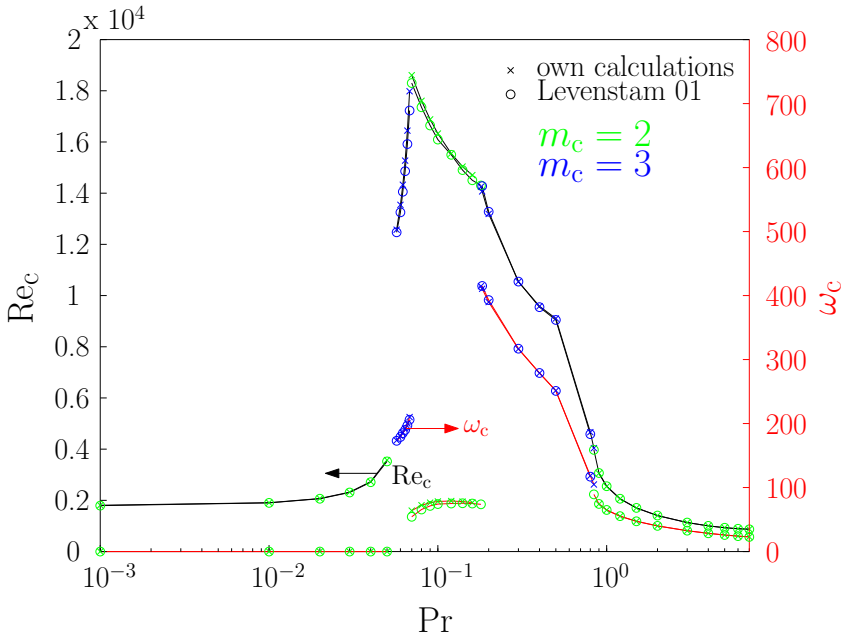

Figure 3.7: Verification of the C-code of `MaranStable`: critical Reynolds number $\mathrm{Re_c}$ and critical frequency $\omega_c = \Im(\gamma_n)$ dependent on Prandtl number Pr.

et al., 2001) and lies within ±1.5 %. The corresponding stability diagram is shown in fig. 3.7.

Another way to test the CG-code of `MaranStable` is a validation test. But idealizing assumptions in computational modeling and measurement uncertainties in experiments prevent perfect predictions. A comparison with an experiment of (Simic-Stefani *et al.*, 2006) lead to satisfactory results. The experiment was done with the fluids acetone/air and the effect of evaporation of acetone on the stability boundaries was investigated. It was discovered that stronger evaporation leads to

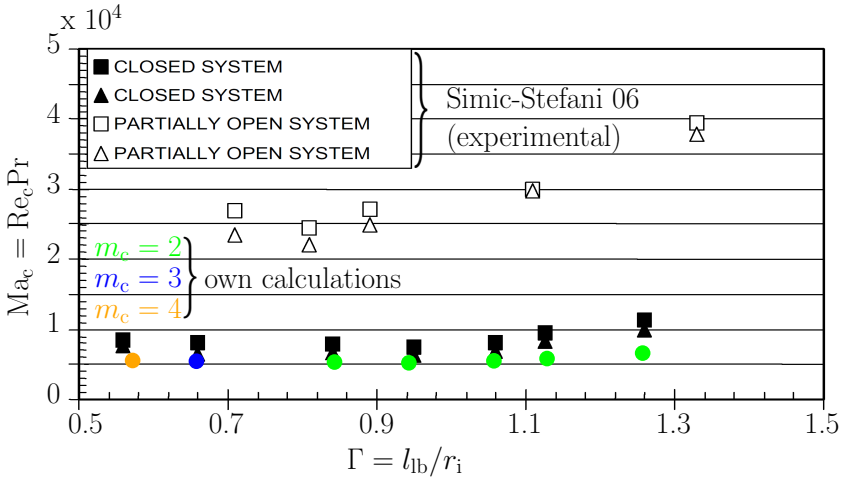

Figure 3.8: Validation of the CG-code of `MaranStable`: critical Marangoni number $\mathrm{Ma_c}$ dependent on the aspect ratio $\Gamma = l_{\mathrm{lb}}/r_{\mathrm{i}}$; Upper disk temperature $T_{\mathrm{hot}} \approx 23 - 25\,^{\circ}\mathrm{C}$ is kept constant, lower disk temperature varies. (squares: ramping up T_{cold}, triangles: ramping down T_{cold}).

Table 3.2: Geometrical parameters for the linear stability analysis.

r_{i} in m	r_{o} in m	l_{in} in m	l_{out} in m
0.0035	0.0065	0.005	0.005

larger critical Marangoni numbers Ma. A stability diagram is shown in fig. 3.8. Calculations are compared with the closed system because the evaporation of acetone is then strongly reduced. Specified parameters for the linear stability analysis are shown in table 3.2 and 3.3. At higher and lower aspect ratios predictions of the linear stability analysis deviates from the experimental data, because of idealizations in the CG-model and relatively large experimental uncertainties. The

Table 3.3: Fluid properties for acetone and air at 23 °C and 101325 Pa.

	ν in $\mathrm{m^2/s}$	ϱ in $\mathrm{kg/m^3}$	λ in $\mathrm{W/m\,K}$	κ in $\mathrm{m^2/s}$	β in $\mathrm{K^{-1}}$	γ in $\mathrm{N/m\,K}$
acetone	4.1×10^{-7}	787	0.16	9.5×10^{-8}	1.43×10^{-3}	12.62×10^{-5}
air	1.54×10^{-5}	1.19	0.026	2.15×10^{-5}	3.38×10^{-3}	–

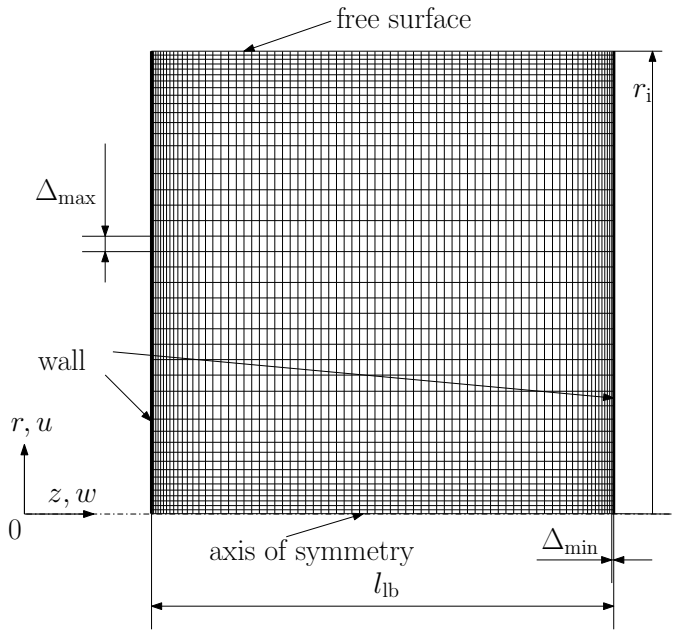

Figure 3.9: Numerical grid with parameters Δ_min and Δ_max for the grid-convergence check. The aspect ratio of the liquid bridge is $\Gamma = 1$.

CG-model only considers a fixed cylindrical shape of the liquid bridge, constant fluid properties and no evaporation of liquid. Whereas in the experiment the surface deformation caused by gravity becomes stronger with increasing aspect ratios. With decreasing aspect ratios the critical temperature difference increases. As a result, the evaporation of acetone and also the effect of temperature dependence of the fluid properties become significant.

To investigate the influence of the numerical grid on stability boundaries a grid-convergence study was carried out. Investigations to follow focus on the behavior of high-Prandtl-number liquids. For those liquids thin thermal boundary layers are expected and have to be resolved by the grid. Stretching factors f (aspect ratio of neighbor cells), minimal and maximal cell sizes (Δ_min and Δ_max) (see also fig. 3.9) of the grid are varied. To be able to carry out computations on very fine grids only single-phase calculations with an adiabatic surface have been conducted. Stability boundaries depending on Pr were calculated on different grids which is shown in 3.10. Grids which are marked with triangles and squares in fig. 3.10 are quite inaccurate when $\mathrm{Pr} > 10$. All other grids would be accurate enough. To ensure that thermal boundary layers will be resolved for the calculations presented below a minimum cell size of $\Delta_\mathrm{min} = 5.00 \times 10^{-5}$ was chosen on all boundaries and the free surface. Because our computational resources are limited in memory to 24 GB maximal 300000 grid cells can be handled for the linear stability analysis. Hence, a relatively large stretching factor $f = 1.1$ and a maximum cell size $\Delta_\mathrm{max} = 500\Delta_\mathrm{min} = 0.025$ is used as a compromise to enable a variation of the geometry parameters in a wide range.

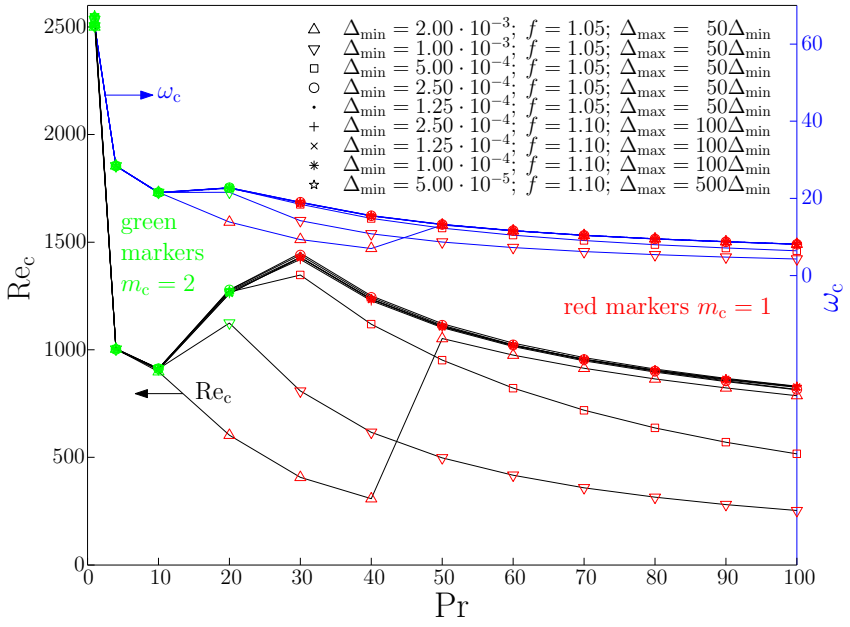

Figure 3.10: Critical Reynolds numbers and frequencies dependent on the Prandtl number for different numerical grids.

It should be noted that energy-conservation checks were also carried out. We found that the normalized residuals were smaller than 10^{-4}. The work in this package is thus completed.

WP B2.3: Compute data by CG-code

To obtain an overview on the characteristics of the gas–liquid coupling a number of simulations were carried out. The first computation was done for the 2D isothermal two-phase flow with viscosity and density ratios representing the system air/water (at 20 °C and 1 bar). From fig. 3.11 it can be seen that the coupling between gas and liquid flow fields through shear stresses is only weak.

Another calculation was made for a 2D axisymmetric thermocapillary flow with the geometry and the fluids as defined in JEREMI project. The boundary conditions are in the range of the experimental parameters for a subcritical flow with $\Delta T = 26\,°C$. For these parameters a 2D axisymmetric flow is expected. The influence of the thermocapillary flow on the gas phase can be seen in fig. 3.12. The stream functions are scaled differently in the liquid and in the gas phase for better visibility. The temperature field is shown in fig. 3.13. The thermocapillary flow causes high velocity gradients in the gas phase, in particular, in the vicinity of the cold corner (stretched zoom in fig. 3.12). This example illustrates that a high grid resolution is required in the vicinity of the cold corner, which causes high computational costs (memory, time).

The inlet boundary conditions of the previous simulation were varied to explore

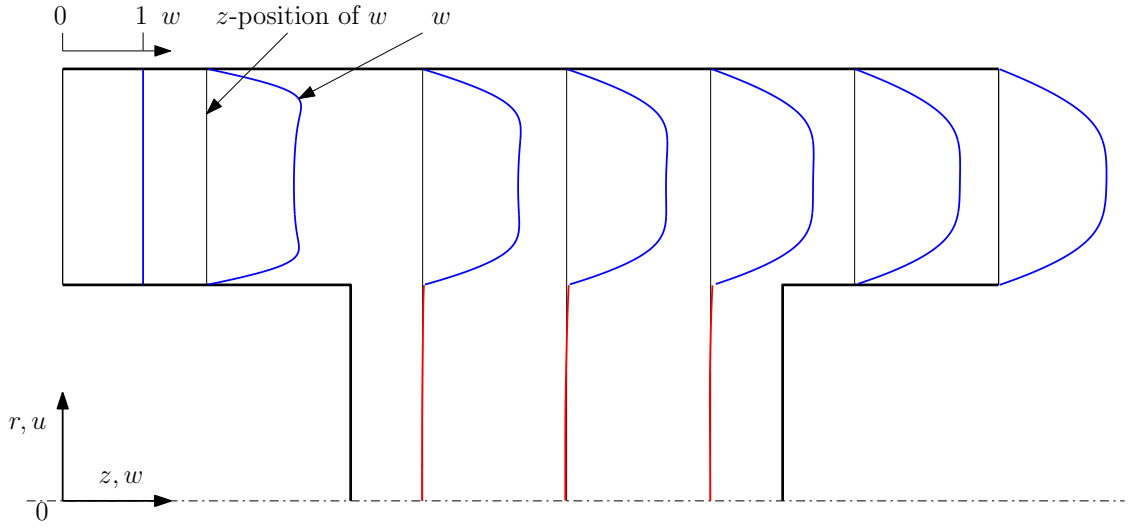

Figure 3.11: Axial velocity profiles for the isothermal two phase flow (blue: air, red: water) for $\mathrm{Re} = 300$, $\nu_\mathrm{g}/\nu_\mathrm{l} = 15$ and $\rho_\mathrm{g}/\rho_\mathrm{l} = 0.001$.

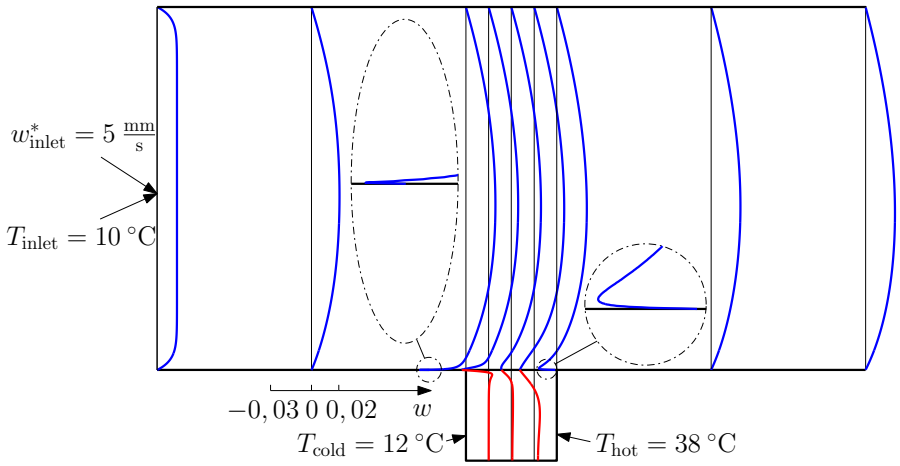

Figure 3.12: Axial velocity profiles for the thermocapillary flow (properties of argon (blue) and silicon fluid "KF-96L-5cs" (red) at $(T_\mathrm{hot} + T_\mathrm{cold})/2 = 25\,^\circ\mathrm{C}$, see table 3.4) for $\mathrm{Re} = 362$, $\mathrm{Pr} = 67$.

their influence on the axial surface velocity, which is an important indicator of the thermocapillary flow. Within the range of experimental parameters the inlet temperature has a much larger effect on the surface-velocity field than the inlet velocity (fig. 3.14).

Finally `MaranStable` was used to calculate stability boundaries for about 6000 sets of parameters. It was started with a reference case for which stability boundaries were calculated varying the gas-inlet velocities. The geometry of the reference case has the following relative dimensions, $l_\mathrm{lb}/r_\mathrm{i} = l_\mathrm{lb}/l_\mathrm{in} = l_\mathrm{lb}/l_\mathrm{out} = 1$ and $r_\mathrm{o}/r_\mathrm{i} = 2$. Fluid properties of the silicon fluid "KF-96L-5cs" and argon were used

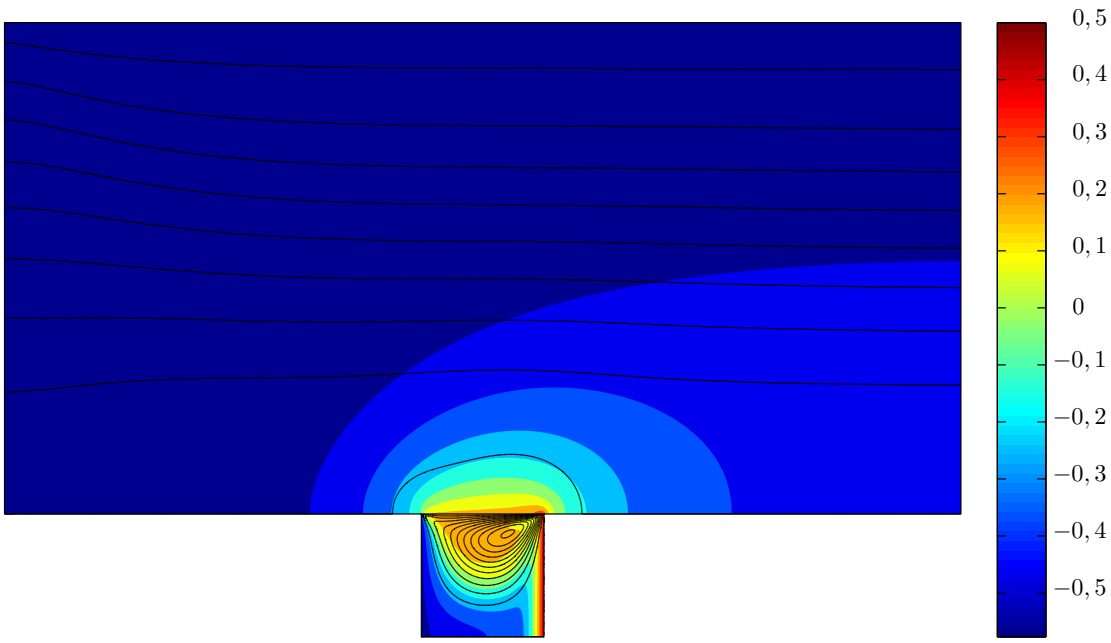

Figure 3.13: Stream functions and temperature field for the thermocapillary flow (properties of argon and silicon fluid "KF-96L-5cs" at $(T_{\mathrm{hot}} + T_{\mathrm{cold}})/2 = 25\,^{\circ}\mathrm{C}$, see table 3.4) for $\mathrm{Re} = 362$, $\mathrm{Pr} = 67$.

(see table 3.4) for the calculations. Boundary conditions as depicted in fig. 3.3 for the basic state and 3.4 for the linear stability analysis were applied. The ambient gas has an enormous effect on the stability boundaries. A stability diagram demonstrating that influence is shown in fig. 3.15 for the reference case. The stability diagram also holds qualitatively for similar geometries, but is depends strongly on the properties of the particular fluids employed. Negative values on the abscissa denote a co-flow. This means that the mean gas flow has the same direction as the surface flow of the liquid. It flows from the hot to the cold site. Positive values denote a a counter-flow situation. The Reynolds number Re (ordinate) is plotted as a function of the product $w^*_{0,\mathrm{in}} l^*_{\mathrm{lb}}$ (abscissa). On the abscissa one could also plot the dimensionless gas velocity $w_{0,\mathrm{in}}$ or an adequate Reynolds number, but there are some disadvantages:

- The dimensionless gas velocity $w_{0,\mathrm{in}} = w^*_{0,\mathrm{in}} l^*_{\mathrm{lb}}/\mathrm{Re}\nu_{\mathrm{l}}$ depends on the thermocapillary Reynolds number. It would be quite difficult to interpret the resulting curve (compare critical curve of fig. 3.15 with the critical curve of fig. 3.16). Different modes are not distinguishable.

- The diagram is just valid for fluids which have the same ratios of density, viscosity, heat conductivity, heat diffusivity, etc., practically just for the used fluid properties. A Reynolds number for the gas flow, e.g., $\mathrm{Re} = w^*_{0,\mathrm{in}} l^*_{\mathrm{lb}}/\nu_{\mathrm{g}}$ could falsely suggest that the calculations would also be valid for different fluids.

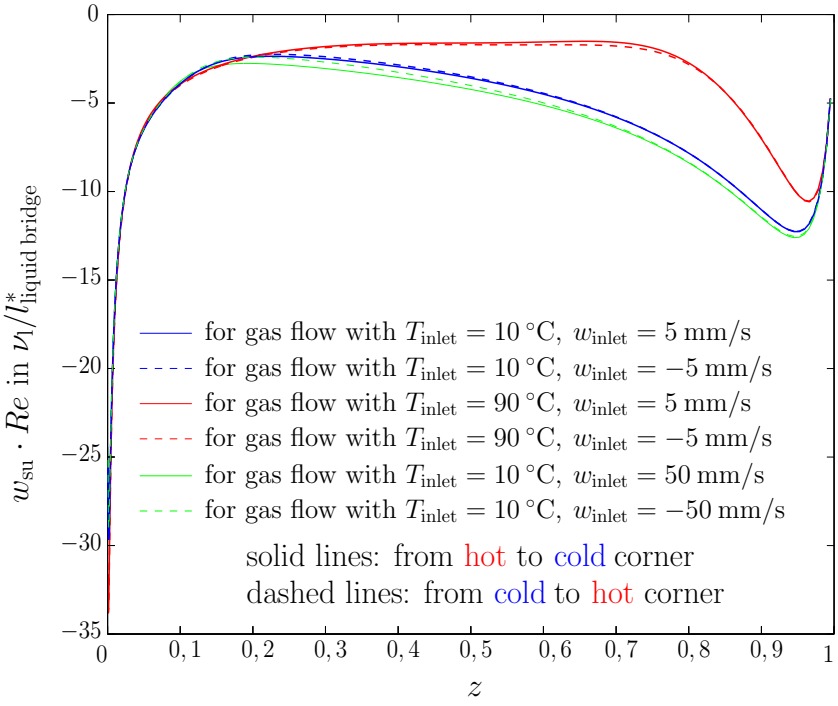

Figure 3.14: Axial surface velocities for thermocapillary flow (properties of argon and silicon fluid "KF-96L-5cs" at $(T_{hot} + T_{cold})/2 = 25\,°C$, see table 3.4) for Re = 362, Pr = 67 and varied inlet boundary conditions.

In fig. 3.15 the different modes are separated with cross markers. Moreover the modes are labeled with the wavenumber m_c and the time-dependence is indicated. If forced gas convection is absent ($w^*_{0,in} = 0\,m/s$) the critical Reynolds number is $Re_c = 558$. Compared to that the critical Reynolds number would be $Re_c = 974$ if the gas phase would be neglected and an adiabatic surface is assumed (horizontal black dash dotted line in fig. 3.15). Thus the forced gas flow has a significant stabilizing effect if a weak gas stream is co-flowing with the thermocapillary flow. In that case the heat loss through the free surface will be decreased or the liquid bridge even heated. In a counterflow the heat loss through the free surface is increased which causes weak destabilization. In the investigated range the gas flow can modify the critical Reynolds number from about 13 to 7000. Remarkable are some regions where an unstable flow can be stabilized with further increasing of the Reynolds number.

Other cases in which a single parameter only is varied with respect to the reference parameters were also considered. One investigation is concerned with the influence of different inert gases on the stability boundaries. The critical curves are shown in fig. 3.17. A significant shift of the stability boundaries is observed. The critical Reynolds number decreases with increasing heat conductivity of the gases if forced gas convection is absent ($w^*_{0,in} = 0\,m/s$). In that case the heat loss through the free surface increases with the heat conductivity of the gases.

Table 3.4: Fluid properties for the silicon fluid "KF-96L-5cs" and different inert gases at 25 °C and 101325 Pa.

	ν in m^2/s	ϱ in kg/m^3	λ in $W/m\,K$	κ in m^2/s	γ in $N/m\,K$
KF-96L-5cs	5×10^{-6}	915	0.12	7.5×10^{-8}	6.37×10^{-5}
argon	1.38×10^{-5}	1.63	0.0176	2.07×10^{-5}	-
helium	1.2073×10^{-4}	0.16394	0.14941	1.7596×10^{-4}	-
neon	3.8189×10^{-5}	0.8248	0.049	5.7675×10^{-5}	-
nitrogen	1.5523×10^{-5}	1.1455	0.025828	2.1664×10^{-5}	-
carbon dioxide	8.3386×10^{-6}	1.7989	0.0165	1.058×10^{-5}	-
sulfur hexafluoride	2.5127×10^{-6}	5.9696	0.0135	3.4316×10^{-6}	-
krypton	7.4155×10^{-6}	3.4252	0.0095	1.1184×10^{-5}	-
xenon	4.3232×10^{-6}	5.3663	0.0056	6.6047×10^{-6}	-

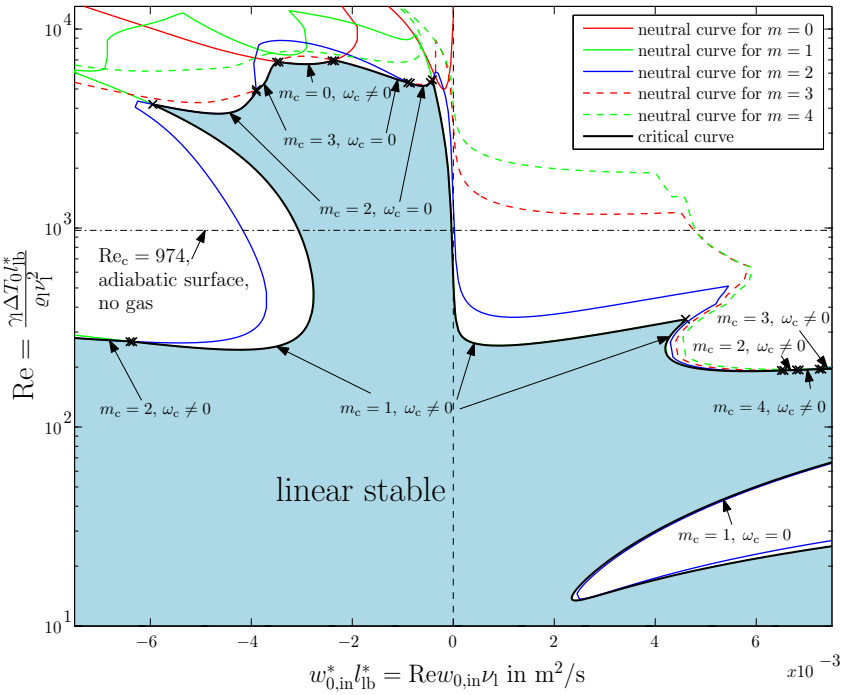

Figure 3.15: Stability diagram for the reference case: Neutral and critical Reynolds numbers Re_c as functions of $w^*_{0,in} l^*_{lb}$.

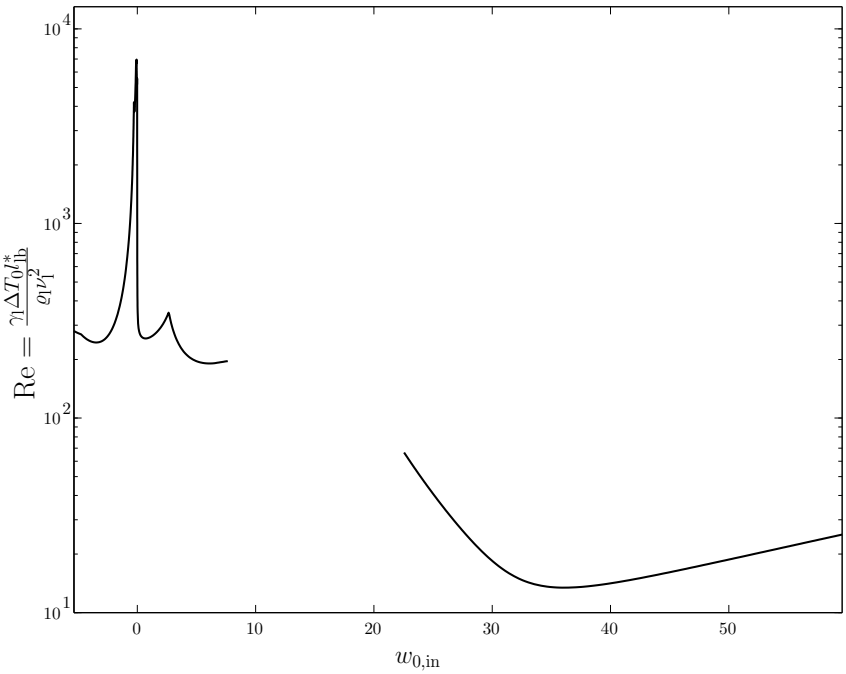

Figure 3.16: Stability diagram for the reference case: Critical Reynolds number $\mathrm{Re_c}$ as function of the dimensionless gas velocity $w_{0,\mathrm{in}}$.

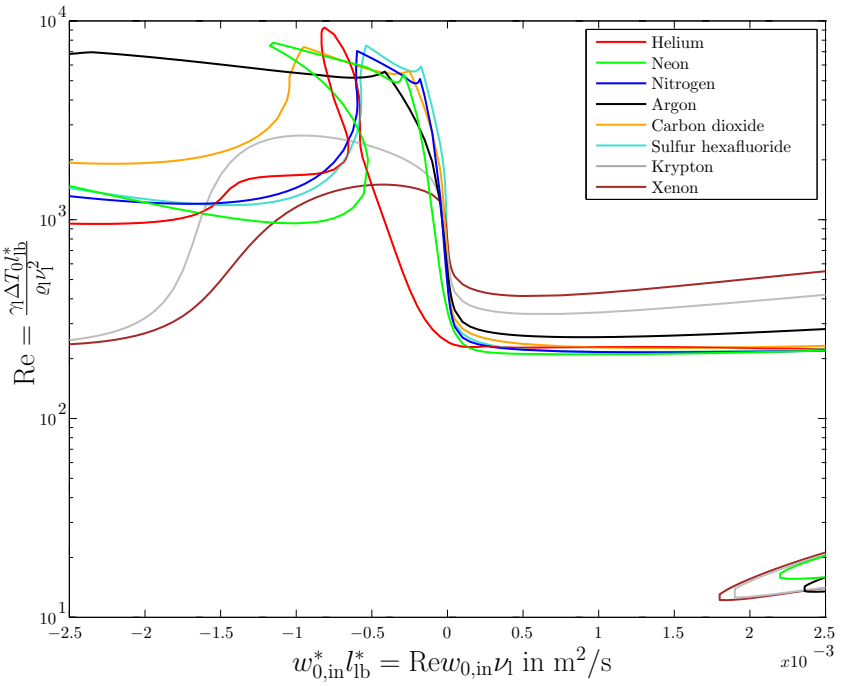

Figure 3.17: Stability diagram for the variation of inert gases: Critical Reynolds number $\mathrm{Re_c}$ as function of $w^*_{0,\mathrm{in}} l^*_\mathrm{lb}$.

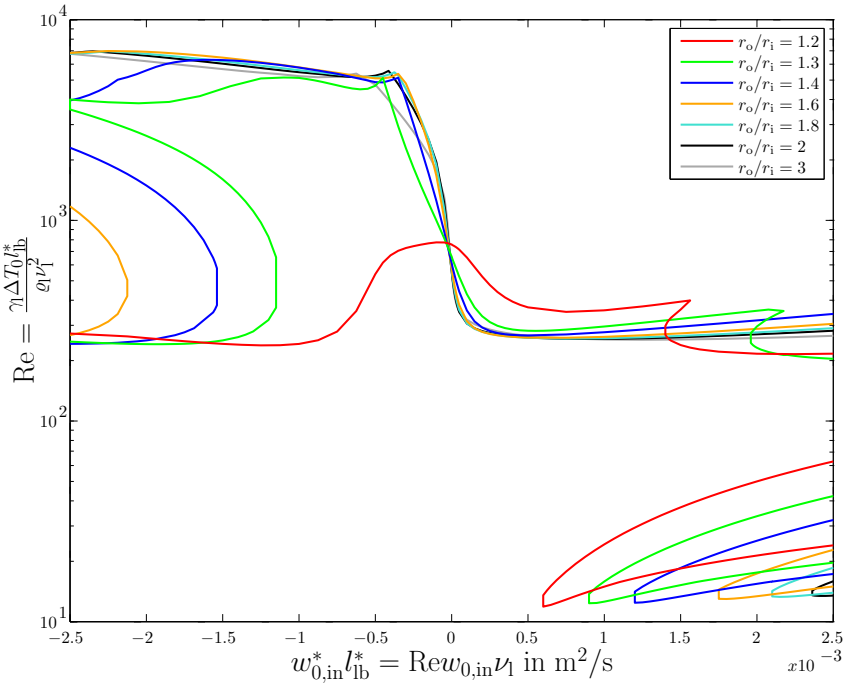

Figure 3.18: Stability diagram for the variation of the aspect ratio of the outer tube radius to the liquid bridge radius $r_\mathrm{o}/r_\mathrm{i}$: Critical Reynolds number Re_c as function of $w_{0,\mathrm{in}}^* l_{\mathrm{lb}}^*$.

The result of varying the aspect ratio of the outer tube radius to the liquid bridge radius $r_\mathrm{o}/r_\mathrm{i}$ is depicted in fig. 3.18. For small aspect ratios, e.g. $r_\mathrm{o}/r_\mathrm{i} = 1.2$, both co- and counterflow of the gas destabilize the flow. Re-stabilization zones are shifted to larger mean gas velocity magnitudes with increasing the radius ratio. Without forced gas convection the critical Reynolds number increases with decreasing aspect ratios.

The influence of the aspect ratios of the liquid bridge length to the inlet/outlet length $l_\mathrm{lb}/l_\mathrm{in} = l_\mathrm{lb}/l_\mathrm{out}$ on the stability boundaries is rather small (see fig. 3.19). Especially for small aspect ratios, where a (nearly) developed gas flow arrives the liquid bridge, which is not very surprising.

The aspect ratio of the liquid bridge length to the radius $\Gamma = l_\mathrm{lb}/r_\mathrm{i}$ has a large influence on the stability of the thermocapillary flow (see fig. 3.20) as well as for the azimuthal wave number m of the critical mode. However a clear correlation between aspect ratio and stability boundary could not be found. It is remarkable, however, that the flow can re-stabilize if $\Gamma \approx 3$, even in the absence of forced gas convection.

To clarify the instability mechanism of the critical modes in fig. 3.15 energy budgets were analyzed. The kinetic energy balance for the ambient gas and the liquid is depicted in fig. 3.21, the thermal energy balance in fig. 3.22. The dominance of $M_{\varphi,\mathrm{g}} + M_{z,\mathrm{g}}$ and the rather small contributions of $I_{\mathrm{v,g}}$ indicate that the transfer of *thermal* (not kinetic) energy of the basic state to the critical mode is responsible

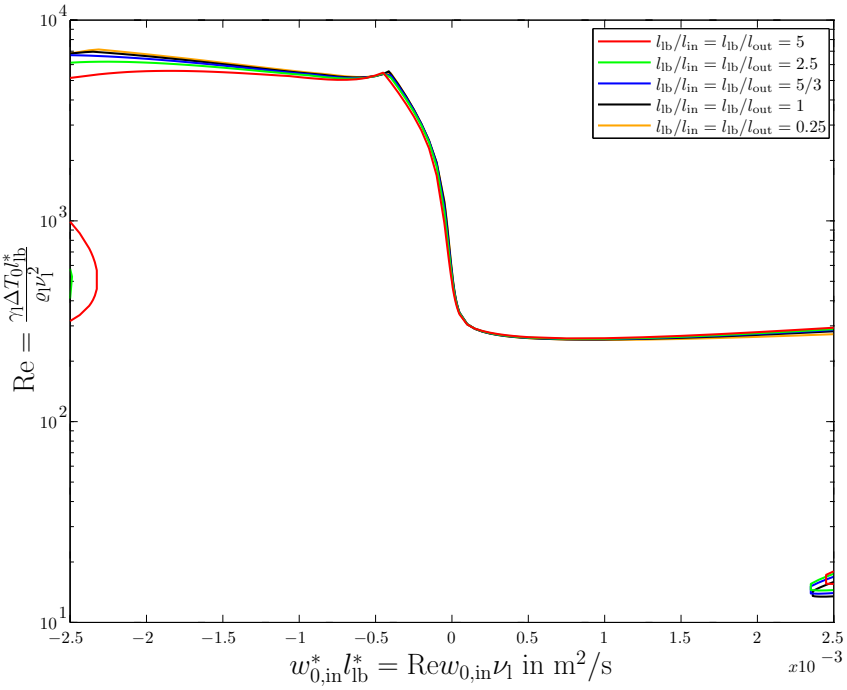

Figure 3.19: Stability diagram for the variation of the aspect ratio of the liquid bridge length to the inlet/outlet length $l_{lb}/l_{in} = l_{lb}/l_{out}$: Critical Reynolds number Re_c as function of $w_{0,in}^* l_{lb}^*$.

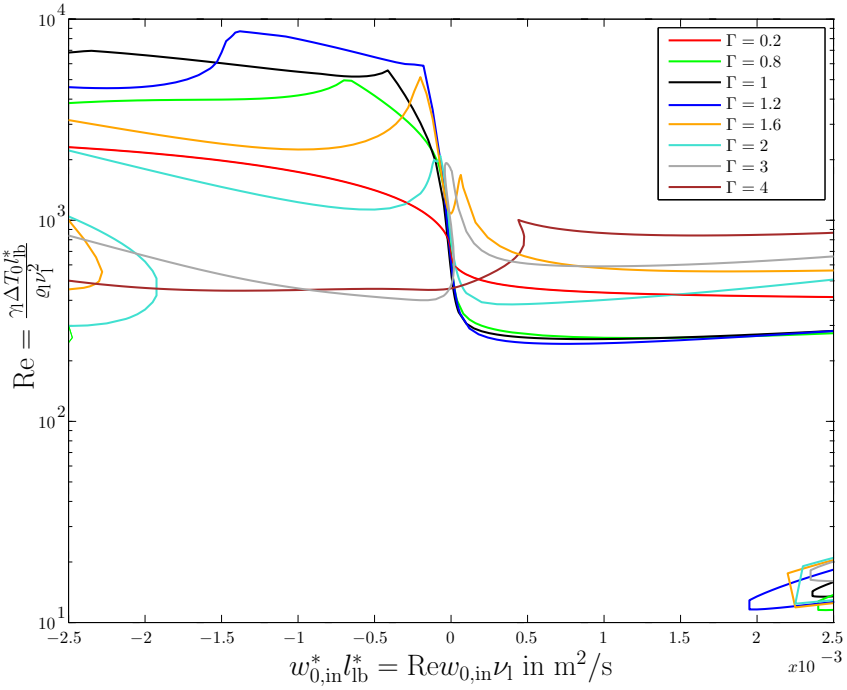

Figure 3.20: Stability diagram for the variation of the aspect ratio of the liquid bridge length to the radius $\Gamma = l_{lb}/r_i$: Critical Reynolds number Re_c as function of $w_{0,in}^* l_{lb}^*$.

for the instability. It can be concluded that the critical flow is a hydrothermal instability. Moreover, the unsteady critical modes are hydrothermal waves. Such an instabilities were first discovered by Smith & Davis (1983) for plane thermocapillary liquid layers and identified by Wanschura *et al.* (1995) for liquid bridges. For high-Prandtl-number liquid bridges, as in the present case ($\mathrm{Pr} = 67$), such a mechanism is typical.

WP B3.1: Program development for 3D stability and the S-model

Changes

25% of the time planned for this work package was shifted to WP B1.1–B2.3 in order to address an unforseen issue (see section 1.2). This WP is 75% completed. An example of the basic state flow and temperature field is depicted in fig. 3.23. V_r denotes the ratio of the liquid volume to the cylinder volume $\pi r_\mathrm{lb}^2 l_\mathrm{lb}$.

WP B3.2: Validation of the S-code

Changes

25% of the time planned for this work package was shifted to WP B1.1–B2.3 in order to address an unforseen issue (see section 1.2). This WP is 75% completed.

WP B3.3: Compute data by S-code

Changes

100% of the time planned for this work package was shifted to WP B1.1–B2.3 in order to address an unforseen issue (see section 1.2). This WP is 0% completed.

WP B4.1: Program development for 3D stability and the SG-model

Changes

25% of the time planned for this work package was shifted to WP B1.1–B2.3 in order to address an unforseen issue (see section 1.2). This WP is 75% completed. A mesh including the gas and liquid phases created by `MaranStable` and showing the deformation of the liquid bridge is given in fig. 3.24. An example of the basic state flow and temperature field is depicted in fig. 3.25.

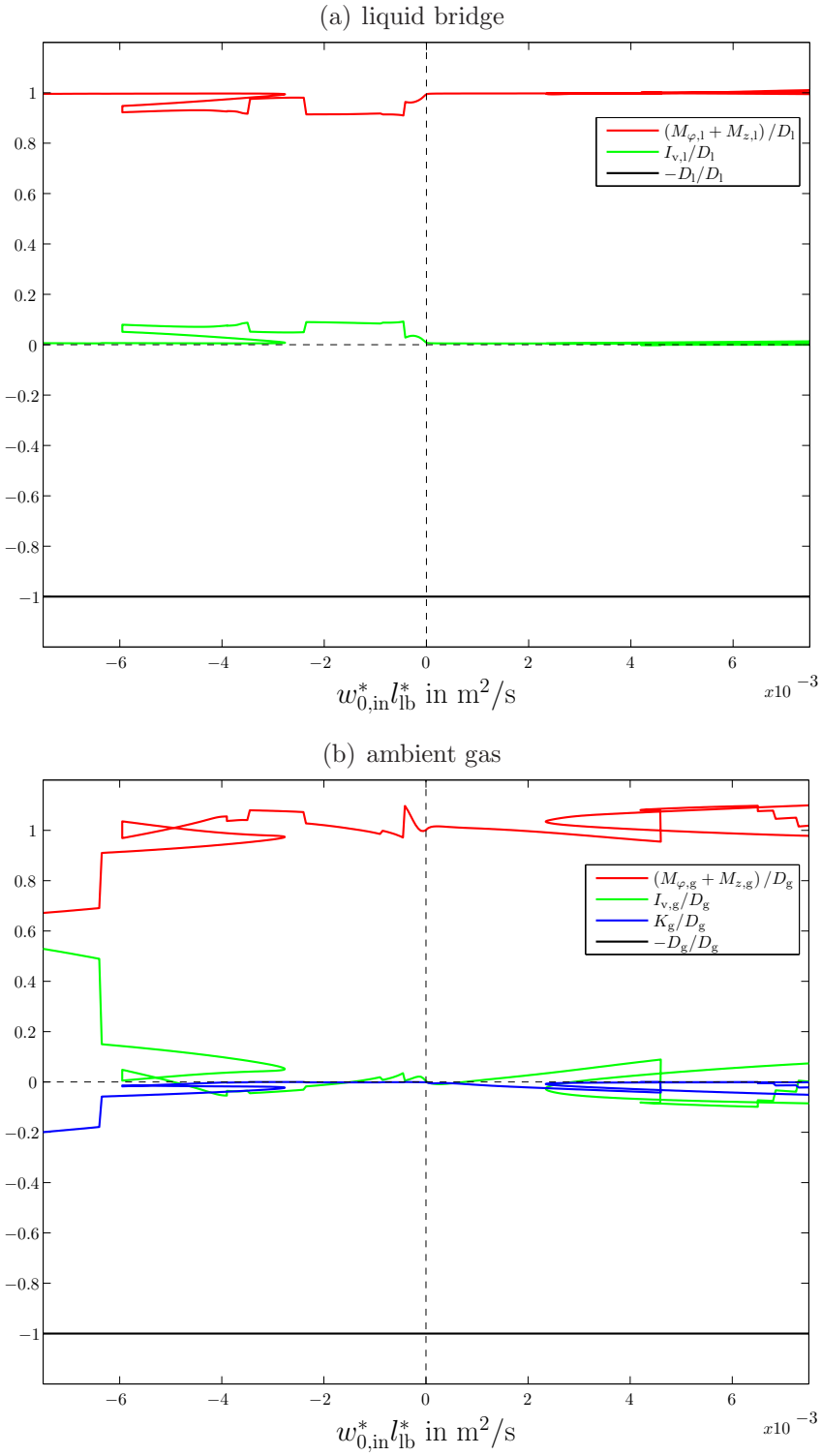

Figure 3.21: Kinetic energy balance.

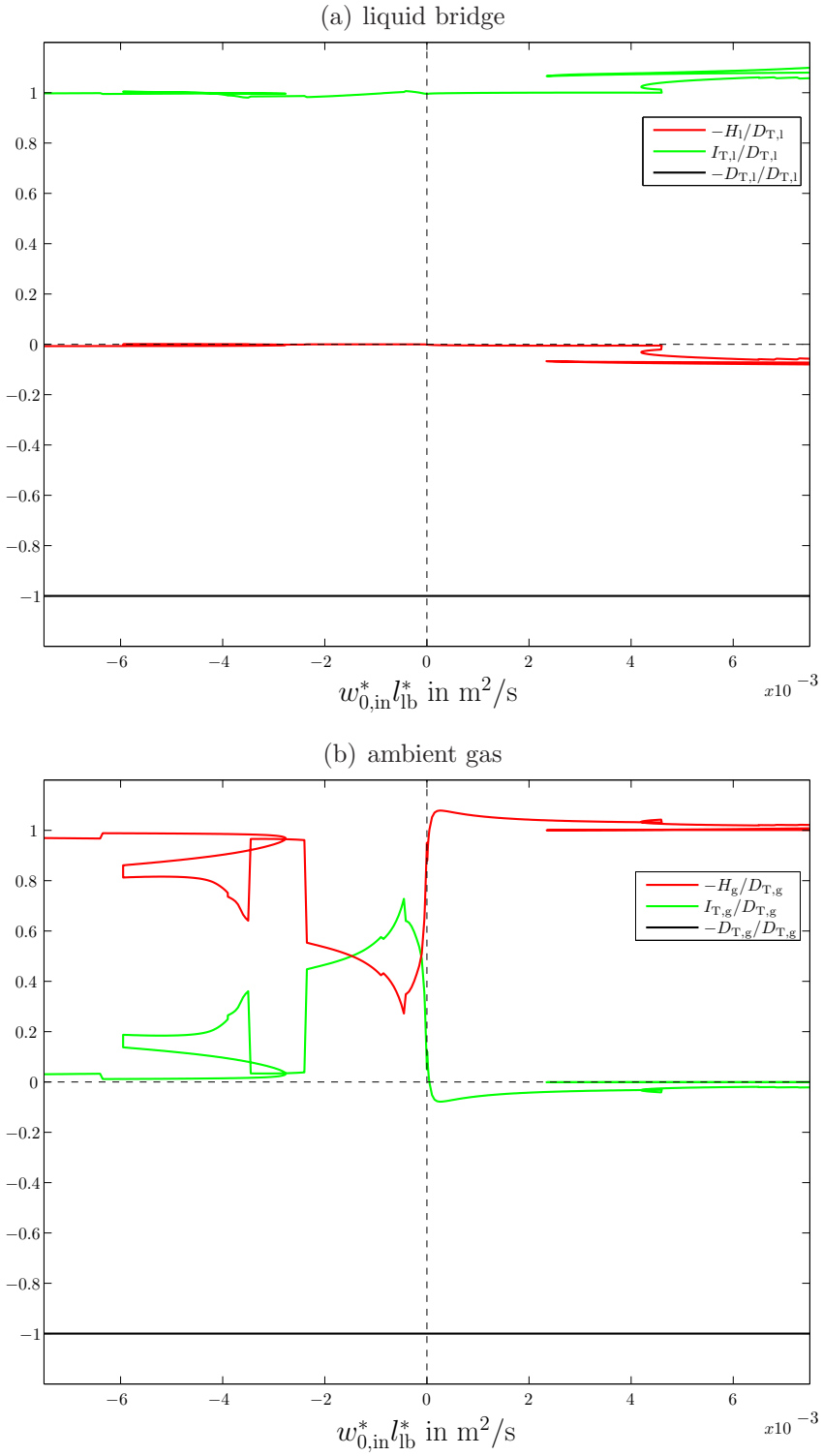

Figure 3.22: Thermal energy balance.

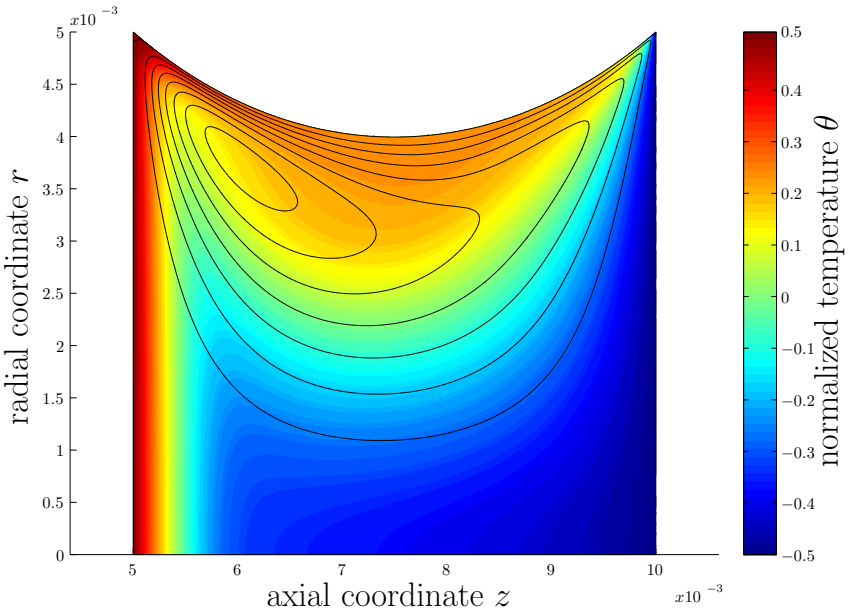

Figure 3.23: Stream functions and temperature field for the thermocapillary flow (properties of the silicon fluid "KF-96L-5cs" at $(T_{\mathrm{hot}} + T_{\mathrm{cold}})/2 = 30\,^{\circ}\mathrm{C}$) in a slender liquid bridge for $V_{\mathrm{r}} = 0.75$, $\mathrm{Re} = 339$, $\mathrm{Pr} = 63$.

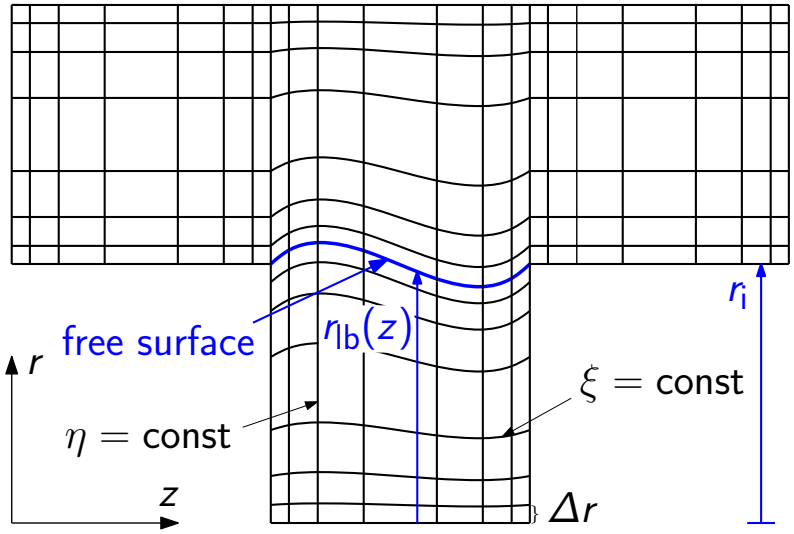

Figure 3.24: Deformed mesh including the gas and liquid phases

WP B4.2: Validation of the SG-code

Changes

25% of the time planned for this work package was shifted to WP B1.1–B2.3 in order to address an unforseen issue (see section 1.2). This WP is 75% completed.

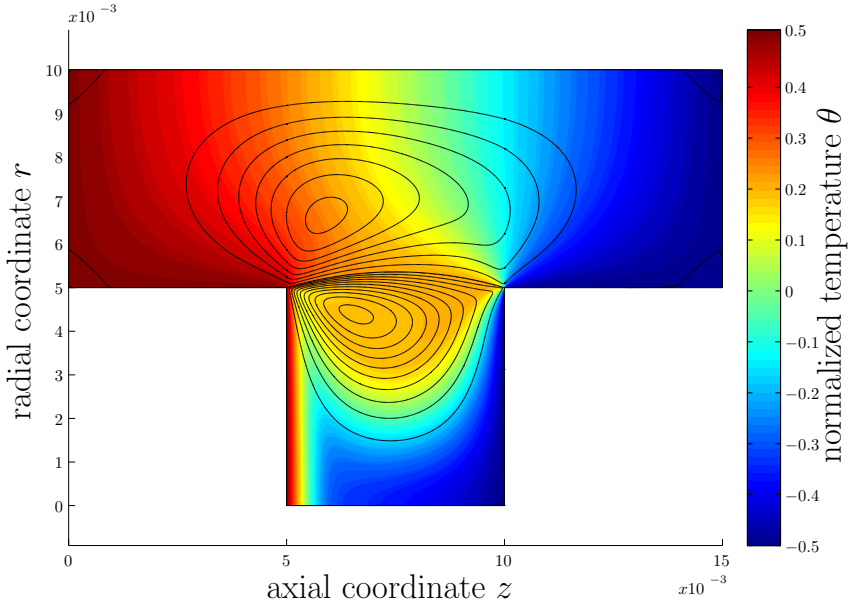

Figure 3.25: Stream functions and temperature field for the thermocapillary flow (properties of argon and silicon fluid "KF-96L-5cs" at $(T_{\mathrm{hot}} + T_{\mathrm{cold}})/2 = 30\,^{\circ}\mathrm{C}$) in a fat liquid bridge for $V_{\mathrm{r}} = 1.1$, $\mathrm{Re} = 339$, $\mathrm{Pr} = 63$.

WP B4.4: Dissemination of results

The results regarding the 2D axisymmetric flow in liquid bridges including the surrounding gas phase were presented at the JEREMI spring meeting on March 5th of 2010 in Brussels (see the section on presentations on page 43). Results regarding the linear stability analysis of the liquid bridge including the surrounding gas phase were presented at the JEREMI fall meeting on October 19th 2010 in Tsukuba (Japan) and at the DFD10 Meeting of The American Physical Society at November 21th in Long Beach (USA, California).

4 C: Particle Accumulation Structures (PAS)

WP C1.1: Literature review for PAS

The literature on PAS and on Lagrangian coherent structures in general is studied permanently.

WP C1.2: Re-writing of PAS code

The computational code for PAS has been completely re-written. It is now available in MATLAB. The particle trajectories are computed using a simplified version of the Maxey–Riley equation Maxey & Riley (1983). To handle the situation in which particles come close or collide with the computational domain a partially elastic reflection model has been implemented for such collisions. To integrate the system of equations the MATLAB solver `ode15s` for stiff systems is being employed using the built-in function `event` for handling particle–boundary collisions. Different interpolation schemes have been tested to compute the flow field at an arbitrary point, including interpolations in physical and in Fourier space.

By transforming the governing equations into a frame of reference rotating with the hydrothermal wave a single snapshot of the flow field of the hydrothermal wave in the liquid bridge is sufficient to compute the particle motion. Using this transformation, we are liberated from simulating the complete flow field parallel to the particle motion. This saves much computing resources.

In the rotating frame of reference the simplified Maxey–Riley equation for zero gravity takes the form

$$\begin{aligned}\ddot{\boldsymbol{y}}' = \frac{1}{\varrho+\frac{1}{2}}\left[-\frac{1}{\mathrm{St}}(\dot{\boldsymbol{y}}'-\boldsymbol{u}')+\frac{3}{2}\boldsymbol{u}'\cdot\nabla'\boldsymbol{u}'\right]- \\ -2\boldsymbol{\Omega}\times\left(\dot{\boldsymbol{y}}'-\frac{3}{2\varrho+1}\boldsymbol{u}'\right)-\boldsymbol{\Omega}\times(\boldsymbol{\Omega}\times\boldsymbol{y}')\left(1-\frac{3}{2\varrho+1}\right).\end{aligned} \tag{4.1}$$

Here $\boldsymbol{y}'$ is the location of the center of mass of the particle in the rotating frame, $\boldsymbol{u}'$ the stationary flow field of the hydrothermal wave in the rotating frame, $\varrho = \rho_\mathrm{p}/\rho_\mathrm{f}$ the ratio of the particle to the fluid density, $\boldsymbol{\Omega}$ the angular velocity of the hydrothermal wave. Using the viscous velocity scale of the thermocapillary flow

$U_0 = \nu/d$ the Stokes number is $\mathrm{St} = 2a^2U_0/(9\nu d) = 2a^2/(9d^2)$, where ν is the kinematic viscosity, a the radius of the particle, and d the height of the liquid zone.

If one considers density matching between fluid and particle the equations simplify to

$$\ddot{\boldsymbol{y}}' = -\frac{2}{3\mathrm{St}}(\dot{\boldsymbol{y}}' - \boldsymbol{u}') + \boldsymbol{u}' \cdot \nabla' \boldsymbol{u}' - 2\boldsymbol{\Omega} \times (\dot{\boldsymbol{y}}' - \boldsymbol{u}')\,. \tag{4.2}$$

In case of velocity matching between particle and fluid at the beginning $t = 0$ the equations for the particle simplifies to the one for a passive tracer

$$\dot{\boldsymbol{y}}' = \boldsymbol{u}'. \tag{4.3}$$

WP C3.1: PAS patterns

For the development of the MATLAB code for PAS we used flow states computed using the existing code Poseidon written by Jens Leypoldt (see Leypoldt *et al.*, 2000). As a standard test case we considered aspect ratio $\Gamma = d/R = 0.66$, Prandtl number $\mathrm{Pr} = 4$, a supercritical Reynolds number $\mathrm{Re} = 1800 \approx 1.67 \times \mathrm{Re_c}$, zero gravity and adiabatic conditions at the free surface $\mathrm{Gr} = \mathrm{Bi} = 0$ (see also fig. 2.1). Under these conditions the flow arises in form of a pure traveling hydrothermal wave with azimuthal wave number $m = 3$.

We found that nearly all particles which have undergone at least a single free-surface collision are transferred to a PAS. An example is shown in fig. 4.1 in comparison with an experimental result of Schwabe *et al.* (2007). Hence, we have shown that PAS can be reproduced numerically. However, the physical mechanism cannot be derived from a pure computational result or from pure observations. Therefore, a more detailed analysis has been performed on the mechanism (see WP C4.2).

Progress for this work package is slightly delayed, because due to the results obtained, much attention has been devoted to the mechanism of PAS formation (see WP C4.2). The insight gained so far indicates that PAS depends on the existence of very fine invariant stream tubes in the rotating frame of reference. In order to reliably compute PAS with numerical flow simulations, the flow near the free surface on the length scale of the particles radius must be reliably resolved. This requires extremely high-resolved three-dimensional time-dependent flow states. As a first step it is tried to meet this requirements for our reference case of $\mathrm{Pr} = 4$ with cylindrical and adiabatic free surface. These computations are currently being carried out.

Changes

There is some delay due to the extremely high accuracy requirements for the numerical solution.

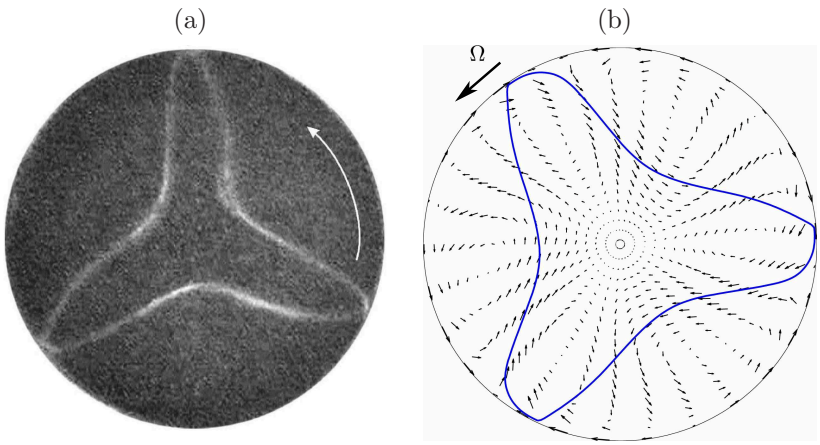

Figure 4.1: (a) Axial view of PAS with period $m = 3$ in an experiment of Schwabe *et al.* (2007) and (b) numerical result for L_{PAS} (full blue line) for nearly passive tracers with very small Stokes number $\mathrm{St} = 5 \times 10^{-5}$ and for $\mathrm{Re} = 1800$.

WP C4.1: Coding for physical mechanism of PAS

Various MATLAB codes have been developed to study various problems associated with the mechanism of PAS. Among these are codes which release particles from dedicated spatial positions, the search for closed streamlines in a numerically given discrete three-dimensional flow field, Poincaré maps for particle returns to certain planes, and various iterated maps designed to study the effect of particle–free-surface collisions.

WP C4.2: Physical mechanism of PAS

Due to the reduced funding (from 24 to 18 months), the time devoted to this WP has been reduced from 5 to 2 months (see chart on page 41 of the proposal).

Based on the experimental finding of Schwabe *et al.* (2007) and our computation of PAS (see WPs C3.1 and C4.1) we have developed the hypothesis that PAS is essentially due to the collision of the particle with the free surface. To that end we considered density-matched particles, because these particles need the least time to form PAS (Schwabe *et al.*, 2007). The passive advection in an incompressible flow cannot, however, lead to particle accumulation. Thus another process is mandatory for it, either inertia or another effect.

To test this hypothesis that surface collisions are key to PAS we assume that the particle is density-matched to the liquid and transported like a passive tracer. However, without any further effect, passive tracers cannot segregate in an incompressible flow. This is obvious and it is well known that Lagrangian coherent structures are due to the inertia of the particles. Thus a mechanism is required that transfers the particle from one stream line to another. Such a process is the

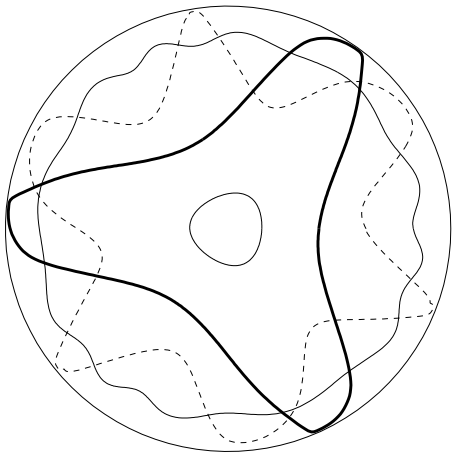

Figure 4.2: Closed streamlines in the rotating frame of reference as viewed in axial projection.

free-surface collision.

Using the above standard reference case we computed the hydrothermal wave until the flow became steady in the frame of reference rotating with the wave. This flow becomes steady in a rotating frame of reference in which the particle motion is then considered by integrating pure advection (no inertia effects) but assuming a finite size of the particles with radius a. We have found PAS in the numerically computed Navier–Stokes flow. The pattern and the time scale of formation does agree with the experimental observations of Schwabe *et al.* (2007). However, due to the extremely tight resolution requirements long-term computation of particle trajectories are difficult and the numerical results could certainly be improved.

The basic result of this work package is that PAS depends strongly on the topological properties of the flow. We found that the steady flow (of the hydrothermal wave) in the rotating frame of reference exhibits regular and chaotic streamlines. In other words, the steady flow exhibits Hamiltonian chaos. We have identified several closed streamlines (for examples, see fig. 4.2) which are surrounded by regular streamlines forming invariant stream tubes. These invariant structures are embedded in a chaotic sea of streamlines. It was found that PAS is possible if one of the invariant regular stream tubes approaches the free surface locally up to a distance which should be of the order of the particles radius. A low-resolution example is shown in fig. 4.3.

Under this condition particles which are passively advected along streamlines can collide with the free surface. This collision is due to the fact that free-surface deformations are practically impossible on the small length scale of the particle size due to the high restoring Laplace pressure. If the streamline on which the particle travels approaches the free surface with a distance less than the particle radius, the particle can no longer follow the flow and will be displaced from one streamline to another. This displacement process has been explained in detail by Kuhlmann & Hofmann (2011) and Hofmann & Kuhlmann (2011). An iterative map has been

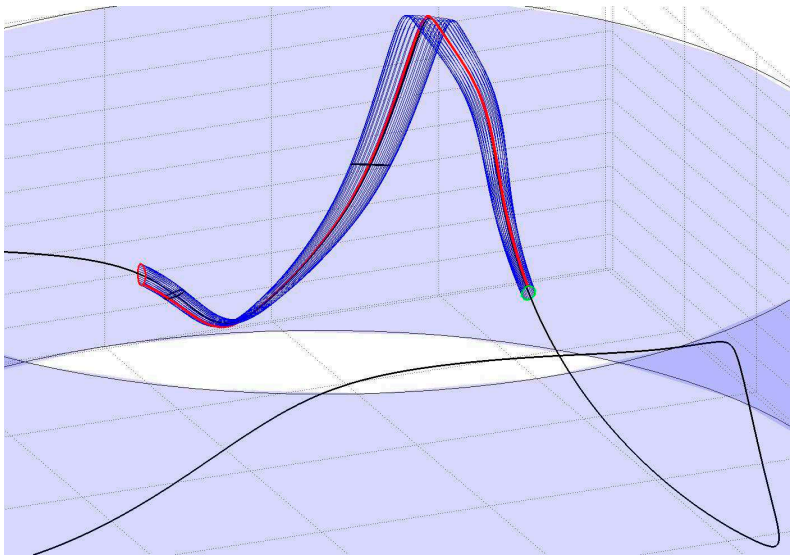

Figure 4.3: Example for a streamtube around a closed streamline in the flow of a hydrothermal wave in the rotating frame of reference. Shown is a close-up of the closed streamline (black) and streamlines (blue) which emerge from a small circle (green) about the closed streamline. The stream tube is shown for one period of the flow which as an azimuthal wave number $m = 3$. One can recognize the radial squeezing of the tube near the free surface (light blue).

developed which qualitatively describes the accumulation process by a simple two-dimensional map of the release point (x_n, y_n) of the particles from the free surface after a collision has taken place. The map consists of a rotation (winding about the closed streamline) and a projection (collision process) (Hofmann & Kuhlmann, 2011). This work has clarified one plausible mechanism of PAS. The basic form of the map reads (assuming a circular cross section of the stream tube near the free surface)

$$x_{n+1} = x_n \cos\theta - y_n \sin\theta, \tag{4.4a}$$

$$y_{n+1} = \min\left[A, x_n \sin\theta + y_n \cos\theta\right]. \tag{4.4b}$$

Here θ represents the winding angle (assumed constant in the model) about a closed invariant stream tube between two successive returns of the particle to the free surface and A is a measure of the distance between $R^* = R - a$, where R is the radius of the liquid bridge and a the particle radius, and the most radial locus of the closed streamline. For $A > 0$ this map has the stable fixed point

$$(x^*, y^*) = \left[-\frac{A}{\tan(\theta/2)}, A\right]. \tag{4.5}$$

The full, closed streamline in fig. 4.2 represents PAS if this closed streamline is tangent to the cylindrical surface $r = R^*$. If the closed streamline intersects with $r = R^*$ PAS is slightly different from the closed streamline. Finally, if the closed

streamline does not intersect with $r = R^*$ but the largest invariant stream tube intersects with $r = R^*$, PAS arises in a tubular form.

Further analyses taking into account particle inertia have shown that coherent Lagrangian structures can exist in the hydrothermal-wave flow. However, the time scale for inertial migration of the particles is orders of magnitude larger than the time scale on which PAS forms by repeated surface collisions. It is thus concluded that PAS indeed results from repeated free surface collisions. For further details we refer to Kuhlmann & Hofmann (2011) and Hofmann & Kuhlmann (2011).

WP C4.4: Dissemination of results

We have published a paper on the PAS mechanism (Kuhlmann & Hofmann, 2011) and another paper has been accepted by the Physics of Fluids (Hofmann & Kuhlmann, 2011). Another paper intended for Physical Review Letters is nearly finished. All works are provided as attachments to this report. Further presentations are planned for the ELGRA Meeting 2011 in Antwerp.

Publications and presentations

Publications

1. H. Kuhlmann and E. Hofmann, The mechanics of particle accumulation structures in thermocapillary flows, The European Physical Journal – Special Topics **192** (1), 3–12 (2011).

2. E. Hofmann and H. Kuhlmann, Particle accumulation on periodic orbits by repeated free surface collisions, The Physics of Fluids **23**, 0721106-1–0721106-14 (2011).

3. H. C. Kuhlmann and Frank M. Muldoon, Particle-accumulation structures in periodic free-surface flows: Inertia versus surface collisions (submitted to Physical Review E).

4. M. Lukasser, K. Nishino and H. C. Kuhlmann, Thermocapillary flow instability in liquid bridges under weighlessness: Experiments and numerical stability analysis (in preparation).

Presentations

1. E. Hofmann and H. Kuhlmann, On the mechanisms of PAS in thermocapillary liquid bridges, JEREMI Meeting of the International Topical Team on Marangoni Convection, Vienna, November 8–10, 2009.

2. E. Hofmann and H. Kuhlmann, A model for PAS, JEREMI Meeting of the International Topical Team on Marangoni Convection, Brussels, March 4–6, 2010.

3. M. Lukasser and H. Kuhlmann, Steady 2D axisymmetric simulation of a liquid bridge including a surrounding gas phase, JEREMI Meeting of the International Topical Team on Marangoni Convection, Brussels, March 4–6, 2010.

4. E. Hofmann and H. Kuhlmann, Particle accumulation in thermocapillary flows, Spring meeting of the ADA Pilot Center of ERCOFTAC, Graz, April 30, 2010.

5. E. Hofmann and H. C. Kuhlmann, The mechanics of particle accumulation structures in thermocapillary flows, 5th Conference of the International Marangoni Association, Firenze, June 7–10, 2010.

6. F. Muldoon and H. C. Kuhlmann, Control of hydro-thermal waves in a Marangoni and buoyancy driven flow using a gradient-based control strategy, IMA5 conference, Florence (2010).

7. H. Kuhlmann and E. Hofmann, Particle accumulation on periodic orbits by repeated free-surface collisions, 8th Euromech Fluid Mechanics Conference, Bad Reichenhall, September 13–16, 2010.

8. M. Lukasser and H. Kuhlmann, Thermocapillary convection in a liquid bridge influenced by an ambient gas: Linear stability boundaries, JEREMI Meeting of the International Topical Team on Marangoni Convection, Tsukuba (Japan), October 18–20, 2010.

9. M. Lukasser, D. Lanzerstorfer and H. C. Kuhlmann, Thermocapillary convection in a cylindrical liquid bridge – Effect of the ambient gas, Bulletin of the American Physical Society **55** (16), ID: BAPS.2010.DFD.EY.6 (2010).

10. E. Hofmann and H. C. Kuhlmann, A model for particle accumulation of density-matched tracers in thermocapillary flows, Bulletin of the American Physical Society **55** (16), ID: BAPS.2010.DFD.AV.1 (2010).

11. M. Lukasser and H. Kuhlmann, A discretizion strategy for a deformed liquid bridge, JEREMI Meeting of the International Topical Team on Marangoni Convection, Brussels, March 7–8, 2011.

12. F. Muldoon and H. Kuhlmann, Modeling of liquid bridges using OpenFOAM©, JEREMI Meeting of the International Topical Team on Marangoni Convection, Brussels, March 7–8, 2011.

13. M. Lukasser and H. C. Kuhlmann, Effect of an ambient gas on thermocapillary convection in high-Prandtl-number liquid bridges, 4th International Symposium on Physical Sciences in Space, Bonn, Germany, July 11–15 (2011).

14. F. Muldoon and H. C. Kuhlmann, Investigation of particle accumulation structures in zero-gravity liquid-bridges, ELGRA Biennial Symposium and General Assembly, Antwerp, Sep. 6–9 (2011).

15. M. Lukasser, H. C. Kuhlmann, Effect of an ambient gas on thermocapillary convection in high Prandtl number liquid bridges, ELGRA Biennial Symposium and General Assembly, Antwerp, Sep. 6–9 (2011).

Posters

16. F. H. Muldoon and H. C. Kuhlmann, Simulations of a liquid bridge with external gas flow, 4th International Symposium on Physical Sciences in Space, Bonn, Germany, July 11–15 (2011, poster).

.

Bibliography

Darbandi, M., & Schneider, G. E. 1998. Numerical Study of the Flow Behavior in the Uniform Velocity Entry Flow Problem. *Numerical Heat Transfer, Part A: Applications: An International Journal of Computation and Methodology*, **34**(5), 479–494. 19

Gottlieb, Robert G.; Thompson, Blair F. 2010. Bisected direct quadratic regula falsi. *Applied Mathematical Sciences*, **4**, 709 – 718. 16

Hofmann, Ernst, & Kuhlmann, Hendrik C. 2011. Particle accumulation on periodic orbits by repeated free surface collisions. *Phys. Fluids*, **23**, 0721106–1–0721106–14. 40, 41, 42

Kuhlmann, H. C. 1999. *Thermocapillary Convection in Models of Crystal Growth*. Springer Tracts in Modern Physics, vol. 152. Berlin, Heidelberg: Springer. 20

Kuhlmann, H. C., & Hofmann, E. 2011. The mechanics of particle accumulation structures in thermocapillary flows. *The European Physical Journal Special Topics*, **192**(1), 3–12. 40, 42

Kuhlmann, H. C., Wanschura, M., Rath, H. J., & Yoda, S. 2000. Stability of thermocapillary flows in high-Prandtl-number liquid bridges. *Space Forum*, **6**, 25–30. 21

Lehoucq, R. B., Sorensen, D. C., & Yang, C. 1998. *ARPACK Users' Guide: Solution of Large-Scale Eigenvalue Problems with Implicitly Restarted Arnoldi Methods*. SIAM. 16

Levenstam, Marten, Amberg, Gustav, & Winkler, Christian. 2001. Instabilities of thermocapillary convection in a half-zone at intermediate Prandtl numbers. *Physics of Fluids*, **13**(4), 807–816. 20

Leypoldt, J., Kuhlmann, H. C., & Rath, H. J. 2000. Three-dimensional numerical simulation of thermocapillary flows in cylindrical liquid bridges. *J. Fluid Mech.*, **414**, 285–314. 4, 38

Maxey, M. R., & Riley, J. J. 1983. Equation of Motion for a Small Rigid Sphere in a Nonuniform Flow. *Phys. Fluids*, **26**, 883–889. 37

Meerbergen, K., Spence, A., & Roose, D. 1994. Shift-invert and Cayley transforms for detection of rightmost eigenvalues of nonsymmetric matrices. *BIT Numerical Mathematics*, **34**, 409–423. 10.1007/BF01935650. 16

Muldoon, Frank Herbert. 2004. *Numerical Methods for the Unsteady Incompressible Navier-Stokes Equations and their Application to the Direct Numerical Simulation of Turbulent Flows*. Ph.D. thesis, Louisiana State University. 19, 20

Schwabe, D., Mizev, A. I., Udhayasankar, M., & Tanaka, S. 2007. Formation of dynamic particle accumulation structures in oscillatory thermocapillary flow in liquid bridges. *Phys. Fluids*, **19**, 072102–1–072102–18. 38, 39, 40

Simic-Stefani, S., Kawaji, M., & Yoda, S. 2006. Onset of oscillatory thermocapillary convection in acetone liquid bridges: The effect of evaporation. *International Journal of Heat and Mass Transfer*, **49**(17-18), 3167 – 3179. 21

Smith, M. K., & Davis, S. H. 1983. Instabilities of dynamic thermocapillary liquid layers. Part 1. Convective instabilities. **132**, 119–144. 32

Wanschura, M., Shevtsova, V. S., Kuhlmann, H. C., & Rath, H. J. 1995. Convective instability mechanisms in thermocapillary liquid bridges. *Phys. Fluids*, **7**, 912–925. 16, 32